Title: Microscopic interactions control a structural transition in active mixtures of microtubules and molecular motors

Author list:
Bibi Najma[1], Aparna Baskaran[1], Peter J. Foster[1,2], Guillaume Duclos[1,*]

Affiliations:
[1]Department of Physics, Brandeis University, Waltham, MA 02453
[2]Present address: Department of Physics and Astronomy, University of Southern California, Los Angeles, CA, 90089, USA
[*]gduclos@brandeis.edu

Abstract:
Microtubules and molecular motors are essential components of the cellular cytoskeleton, driving fundamental processes *in vivo,* including chromosome segregation and cargo transport. When reconstituted *in vitro*, these cytoskeletal proteins serve as energy-consuming building blocks to study the self-organization of active matter. Cytoskeletal active gels display rich emergent dynamics, including extensile chaotic flows, locally contractile asters, and bulk contraction. However, it is unclear which protein-scale interactions, if any, set the contractile or extensile nature of the active gel, or how to control the transition from one phase to another in a simple active system. Here, we explore the microscopic origin of the extensile-to-contractile transition in a reconstituted active material composed of stabilized microtubules, depletant, ATP, and clusters of kinesin-1 motors. We show that microscopic interactions between highly processive motor clusters and microtubules can trigger the end-accumulation of motor proteins, which in turn drives polarity sorting and aster formation. Combining experiments and simple scaling arguments, we demonstrate that the extensile-to-contractile transition is akin to a self-assembly process where nematic and polar aligning interactions compete. We identify a single control parameter given by the ratio of the different component concentrations that dictates the material-scale organization into either a contractile aster or an extensile bundle. Overall, this work shows that robust self-organization of cytoskeletal active materials can be controlled by precise biochemical and mechanical tuning at the microscopic level.

Keywords:
Active matter, molecular motors, microtubules, self-organization.

Significance statement:
Self-organization in living cells is often driven by energy-consuming motor proteins that push and pull on a network of cytoskeletal filaments. However, it is unclear how to connect the emergent structure and dynamics of reconstituted cytoskeletal materials to the properties of their microscopic building blocks. Here, we systematically correlate bulk structure with asymmetry of the motor distribution along single filaments to explain the transition from extensile bundles to contractile asters in active networks of stabilized microtubules crosslinked by motor proteins. We combine experiments and scaling arguments to identify a single number

that predicts if the system will self-assemble into bundles or asters. This work shows that both biochemical and mechanical interactions set the emergent structure of active biomimetic gels.

Introduction:

Active materials are far-from-equilibrium materials composed of energy-consuming building blocks [1]. They self-organize into spontaneously moving structures larger than their microscopic components, and their material-scale mechanics emerge from non-equilibrium interactions between active units. In thermodynamically driven self-assembly, the emergent structures are set by the interaction strengths of the various molecules [2]. In active materials, pattern formation often results from dynamical processes whose characteristic time scale sets the emergent structure and dynamics [3]. Rationalizing why active materials spontaneously move in certain ways often relies on determining what symmetries are conserved or broken at the micro and mesoscopic scales. However, coarse-graining microscopic interactions is often challenging, particularly for living systems and biomimetic active matter where molecular interactions are either unknown, non-linear, or too complex to be reduced to a single physical mechanism.

The cellular cytoskeleton is a prototypical example of an active material [4,5]. Cytoskeletal networks are driven away from thermodynamic equilibrium in part by molecular motor proteins. These proteins transduce chemical energy into mechanical work at the molecular scale, collectively driving the self-organization of the cytoskeleton at the cellular level. *In vivo*, these active processes underlie cellular force generation and mechanics [6]. *In vitro*, they provide a blueprint to build active machines endowed with life-like properties, such as the ability to spontaneously flow [7,8], change shape [9-11], or divide [12,13].

Many examples of *in vitro* cytoskeletal materials self-organize into distinct states, which reflect the richness of the microscopic interactions between various molecular motors and cytoskeletal filaments. Important categories of this include materials with bulk extensile [14-16] or contractile and aster-forming behaviors [17-28]. Extensile dynamics have been associated with active systems organized into mesoscopic polymer bundles, frequently through the addition of a depletion agent. Such extensile flows have been reported for both microtubule/kinesin [14] and actomyosin [29,30] based materials. Theoretical work has suggested that extensile stresses could arise from the polarity sorting of filaments [31] or the mechanical properties of the motors themselves [32,33]. Under other conditions, both microtubule and actin-based active gels have been found to undergo bulk contraction. Microtubule bulk contraction has been argued to stem from contractile active stresses generated by the clustering of microtubule ends by end-accumulating motors [17,22,34,35]. Actomyosin contraction is also fundamentally rooted in symmetry-breaking at the filament level, either because of the non-linear mechanical properties of actin filaments [21,36,37], end-accumulation of myosin motors [26,38], or through the asymmetric distribution of crosslinkers or motor proteins [39].

Despite these advances, rationally designing a simple and programmable biomimetic material that could exert both extensile and contractile stresses is still a challenge. Examples of such multifunctional materials can be found in living organisms. The mitotic spindle is a prototypical

example of a self-organized active nematic liquid crystal that exerts extensile stresses at its center and contractile stresses at its poles [40,41]. However, this coexistence is thought to result from the microscopic work of a mixture of motor proteins with opposite directionality and asymmetric crosslinking properties [42]. Recent *in vitro* experiments and simulations show that microtubule networks composed of a mixture of motors with opposite directionality can display either extensile or contractile dynamics depending on the relative concentration of each motor protein [42,43]. In the presence of a single type of end-accumulating motor, competition between microtubule growth rate and motor speed dictates if the bulk dynamics are extensile or contractile [42]. However, most reconstituted active systems composed of stabilized microtubules and a single type of motor display a single bulk organization - either contractile or extensile [14,17,22]. Two recent examples, with clusters of kinesin-1 motors [28,44] and end-accumulating kinesin-4 motors [10], show that networks of stabilized microtubules crosslinked by a single type of motor proteins can display either extensile or contractile dynamics, but the underlying physical or biochemical mechanisms are unclear.

Here, we investigate the microscopic origin of the extensile-to-contractile transition in active gels composed of stabilized microtubules and kinesin-1 motor clusters. We show that the emergent bulk dynamics are related to how processive motor clusters are distributed onto microtubules, with extensile flows when motors' distribution is uniform or aster formation and global contraction if they end-accumulate. We show that end-accumulation can be triggered by either increasing motor cluster concentrations or decreasing ATP concentrations, which is consistent with increasing the lattice-binding rate and decreasing the lattice-dissociation rate of the motor-microtubule binding kinetics. Further, we show that the timescales of the transition from extensile to contractile are correlated with the timescales of end-accumulation at the microscopic scale. Increasing nematic alignment using a depletant, a microtubule-specific crosslinker, or by adding colloidal rods triggers the reversed transition from contractile asters to extensile bundles without impacting motor cluster end-accumulation at the single filament level. Simple scaling arguments demonstrate that the extensile-contractile phase boundary results from the competition between polar sorting and nematic alignment. This self-assembly model allows us to predict the emergent structure based on a single control parameter given by the ratio of the various component concentrations.

Taken together these results elucidate the physical and biochemical mechanisms that underlie the extensile-to-contractile transition in simple active gels composed of stabilized microtubules and highly processive motor clusters. We identified generic microscopic interactions that control structural transitions into bundles or asters by relating the concentrations of motors, ATP, and microtubules to the ability of the clusters to end-accumulate at the single filament level. While experiments with actomyosin and recent simulations demonstrate that microscopic kinetics can modify the mechanics, leading to contraction and further structural changes into asters [21,37,45], we show that kinesin-microtubule gels instead self-assemble into distinct structures depending on how the motors are distributed along the microtubules, either aligned bundles or radially oriented polarity sorted asters, which in turns set the extensile or contractile dynamics. This represents an important step towards designing multifunctional active biomolecular materials.

Results:

In this paper, we investigate how microscopic interactions control the emergent organization of a minimal *in vitro* system composed of microtubules and multivalent clusters of kinesin-1 molecular motors (**Fig. 1A**) [14,46]. GMPCPP-stabilized microtubules are bundled by a non-specific depletant (20kDa PEG, **Fig. 1B**). Motor clusters are composed of tetravalent streptavidin and biotinylated truncated kinesin-1 motors (consisting of the first 401 amino acids of kinesin-1) that spontaneously dimerize to form a processive double-headed motor (**Fig. 1C**). The exact valency and size of these clusters are unknown. These motor clusters can simultaneously bind microtubule pairs and take steps on microtubules upon hydrolysis of adenosine 5'-triphosphate (ATP). This crosslinking and walking motion results in the sliding of adjacent anti-parallel microtubules, collectively driving the whole network out of equilibrium. In this configuration, a microtubule bundle exerts dipolar extensile stresses, pushing fluid along its long axis while pulling fluid along its short axis [1,14,16] (**Fig. 1B**). After an initial instability [9,16,44], the three-dimensional active gel reaches a long-lived out-of-equilibrium steady state, forming a network of extensile microtubule bundles that continuously reconfigure, driving chaotic flows [14] (**Fig. 1D, Video S1**). In this extensile phase, dual-color imaging of the microtubules and the kinesin-1 clusters revealed that the motors are uniformly distributed along the microtubule bundles (**Fig. 1G, H**).

Assembling active gels with increasing motor cluster concentrations led to a radical change in the emergent structure and dynamics of the active gels: above a critical cluster concentration, the active network transitioned from forming an extensile phase into forming a contractile phase, with large microtubule asters coexisting with an extensile background (**Fig. 1E, Video S2**). Dual-color imaging of microtubules and kinesin-1 clusters revealed that the aster cores were enriched with motor clusters (**Fig. 1I, J, Fig. S1**), a generic feature of both actin-based [26,38] and microtubule-based asters, both *in vitro* [10,28,42,47] and in cellular extracts [22,48-50]. Further increasing the motor cluster concentration led to a second transition from a locally contractile aster phase to a globally contractile phase (**Fig. 1F, Video S3**).

While the large-scale dynamics of extensile and contractile active matter are well described by active hydrodynamic theories [51], these coarse-grained models often take the fundamental stress-generating entity as a starting point for estimating how stresses propagate to larger length scales [52]. When the entity is a bundle, it is natural to use a dipolar formulation of active gel hydrodynamics [16,53,54]. When the entity is an aster, it is more appropriate to start from a scalar generator of active stresses that act as a point source driving the flows [22,55]. In both cases, the mechanisms that control the organization of the mesoscale stress-generating entity are outside the scope of such hydrodynamic approaches. Instead, the extensile-to-contractile transition suggests a discontinuity in how the symmetries of the active stress relate to motor concentration, which could be due to either i) unexpected non-linearities that rectify the emergent mechanics of the active gel [45], or ii) concentration-dependent change in the mesoscale organization controlled by the microscopic interactions between motors and microtubules.

To systematically study this transition, we characterized the active gel's extensile or contractile nature for a wide range of ATP and motor cluster concentrations (**Fig. 1K**). The resulting phase diagram reveals that the critical motor cluster concentration that triggers the extensile-to-contractile transition depends on the ATP concentration. While dyneins and many kinesins are known to end-accumulate [56-59], we are unaware of this behavior being reported for kinesin-1 motors. Hence, we first tested if the transition could be due to a stiffening of the network due to an increasing fraction of molecular motors functioning as passive microtubule crosslinkers when ATP is limited. Indeed, kinesin-1 motor clusters are known to have a dual antagonistic role, fluidizing or stiffening the network depending on ATP concentration [9,44,60].

This hypothesis was rooted in a variety of theoretical and experimental work on active gels. Indeed, previous theoretical work showed that non-linear elasticity can rectify the activity of an extensile network, leading to bulk contraction [45,61,62] [Liverpool]. On the experimental side, direct imaging of actin filaments during bulk contraction suggests that the nonlinear mechanical response of actin filaments is responsible for the contractility of disordered actomyosin networks as they resist stretching but easily buckle upon compression [21]. Further, experiments and simulations of crosslinked actomyosin networks showed that for stiff filaments, increasing crosslinking density can trigger a transition from uniaxial extension to biaxial contraction [37].

Based on this list of evidence, we next asked if a change of network rheological properties was responsible for contraction in the active kinesin-microtubule network considered here. To test that hypothesis, we added PRC1, a microtubule-specific crosslinker that mimics the crosslinking effect of kinesin clusters in the absence of ATP (**Fig. S1A, B**) [63-65]. We first assembled active gels without any additional passive crosslinkers in an extensile state close to the extensile-to-contractile boundary. Increasing the concentration of crosslinkers did not change the extensile nature of the active gels (**Fig. S1C**). On the contrary, when the control state was contractile, adding passive crosslinkers triggered the reversed contractile-to-extensile transition (**Fig. S1D**). This was true whether the initial state was in the aster phase or the globally contractile phase. These results suggest that the extensile-to-contractile transition is not due to a stiffening of the active gel caused by motor clusters acting as passive crosslinkers.

Alternatively, perturbing ATP or kinesin cluster concentration could potentially impact how motors interact with, and hence are distributed on, individual microtubules. How motors are distributed on individual microtubules has been proposed to impact the collective organization of active gels [35,66] and end-accumulation of motor proteins has been shown to underlie both aster formation and bulk contractility [17,22]. As the kinesin asters studied here have an enrichment of motors in the aster's core (**Fig. 1J)**, a hallmark of asymmetric motor distribution, we hypothesized that modulating the ATP and kinesin concentrations could change the degree of motor end-accumulation, and hence the system's propensity towards contractility.

To test this hypothesis, we looked at how fluorescent motor clusters are distributed along isolated microtubules (**Fig. 2, Supplementary Materials, section 2a**). We observed that in conditions where the bulk was extensile, motor clusters were uniformly distributed along

microtubules (**Fig. 2B, C**). However, when the concentration of ATP is decreased (**Fig. 2A**) or the concentration of motor clusters is increased (**Fig. 2D**), motor clusters formed dense aggregates on one end of the microtubules and the corresponding bulk dynamics were contractile. We confirmed these trends by quantifying the fraction of microtubules with motor cluster caps for a range of ATP and motor cluster concentrations (**Supplementary Materials, section 4a**). Either decreasing ATP concentration or increasing motor cluster concentration led to an increase in the fraction of microtubules with motor caps (**Fig. 2G, H**). Interestingly, quantitative analysis of cap formation at the single microtubule level, shows that the probability of having a cap increases when microtubule length increases (**Fig. S2E**), suggesting that an antenna model may underlie the cap formation process [58,67]. Bulk experiments performed at fixed tubulin concentration with annealed microtubules with longer average lengths show that annealing can also trigger a transition from extensile to contractile dynamics (**Fig. S2A-D**). Furthermore, decreasing the microtubule density without changing the microtubule length distribution also triggers a transition from extensile to contractile dynamics for PEG-based active gels (**Fig. S3A**). However, as the number density of microtubules decreases as their length increases during annealing, we cannot conclude if the bulk self-organization depends on the microtubule length.

Inspired by experiments and theory describing the mechanisms that underlie end-accumulation of highly processive Kip3 motors on microtubules [58], we hypothesize that the processivity of the kinesin-1 motor clusters is a key feature that enables the formation of motor caps and the resulting extensile-to-contractile transition. In Leduc et al. [58], a phase diagram is proposed where motor end-accumulation is controlled by the motor's end-dissociation rate and the density of motors on microtubules. However, the authors argue that kinesin-1 motors under physiological conditions should not end-accumulate due to their low processivity and high end-dissociation rate. This apparent discrepancy with the present results can be reconciled when considering that increased valency of motor clusters can lead to higher processivity [68]: to unbind from the microtubule lattice, all kinesin heads in the cluster must be simultaneously unbound, which becomes less probable as the valency of the cluster increases. In our single microtubule experiments, clusters of K401 kinesin-1 can have runs longer than 4µm (**Figs. S4B**), while the run length of dimeric kinesin-1 is closer to 1 µm [69]. Here, the exact valency of the motor clusters is unknown, despite the 2:1 stoichiometric ratio of single-headed motors to streptavidin. Indeed, K401 kinesin-1 motors can spontaneously dimerize, thus potentially presenting two biotins that could each bind to a different streptavidin, which could in turn bind additional motors (**Fig. S4A**). Dimerized K401 motors in the absence of a streptavidin linker do not end-accumulate (**Fig. S5**), possibly because of the lower processivity of the single motor compared to multivalent motor clusters [68].

Interestingly, multivalent clusters of non-processive truncated kinesin-1 motors (K365, **Fig. S6A**) can drive both extensile or contractile bulk dynamics, following the same trends for the extensile-to-contractile transition with respect to ATP and motor cluster concentrations. We first identified the aster phase at a higher concentration of clusters with single-headed K365 compared to active gels prepared with clusters of K401 dimers (**Fig. S6B**). Single microtubule experiments confirmed that the clusters of non-processive kinesin-1 were processive and end-accumulated in conditions where bulk dynamics were contractile (**Fig S6 C-E**). To further

263 confirm the importance of high processivity, we increased the dissociation rate of the motor
264 clusters by increasing the concentration of salt. We observed a transition from contractile to
265 extensile bulk dynamics (**Fig. S7A, B, E, F**). Additionally, motor clusters were found to not end-
266 accumulate when salt concentration was increased (**Fig. S7C, D, G, H**).
267
268 To truly test non-processive clusters, we leveraged a recently developed light-activable K365
269 kinesin-1 motor protein [70]. Each motor presents either an iLid or a micro tag which dimerizes
270 when exposed to blue light [25,71] (**Fig. S8A**). Importantly, we think that these motors cannot
271 spontaneously dimerize, similarly to conventional K365 motors. Further, as these motor
272 clusters do not contain streptavidin linkers, the valency of the clusters is limited - by design - to
273 two single-headed non-processive motors. Recent experiments showed that in the presence of
274 depletant, these motor clusters can bind to adjacent microtubules and slide them apart,
275 forming an extensile network [70]. Here, we performed bulk experiments in the absence of
276 depletant to test the ability of these motor dimers to form asters. We combined stabilized
277 microtubules with iLid and micro-conjugated K365 motors and continuously exposed the
278 sample to blue light. While all the other kinesin-1 clusters tested assembled microtubules into
279 asters (including light-activated iLid/micro clusters of processive K401 [25]), we never observed
280 the formation of asters with iLid/micro-K365 motor dimers even for motor concentrations up to
281 three times what was reached with conventional streptavidin-enabled K365 clusters (**Fig. S8B**).
282 Assembling active samples with an increasing amount of non-specific depletant recovered the
283 extensile dynamics previously reported for active gels driven by iLid/micro dimers of non-
284 processive K365 (**Fig. S8B**) [70].
285
286 Taken together, these results suggest that the binding and unbinding kinetics of processive
287 motor clusters dictates if motors will be uniformly distributed or end-accumulate onto
288 microtubules (**Fig. 2I**), which in turn controls in part the transition from contractile asters to
289 extensile bundles. Indeed, decreasing the concentration of ATP leads to a lower dissociation
290 rate k_{off} [69], while increasing the concentration of motor clusters increases the concentration
291 of motors bound to microtubules, and hence a higher association rate, k_{on}. Both mechanisms
292 are known to favor the end-accumulation of highly processive motors [58].
293
294 To further examine the causal link between the formation of motor-rich microtubule end caps
295 and the formation of contractile asters, we compared the dynamics of both processes (**Fig. 3**).
296 Close to the contractile-to-extensile phase boundary, asters do not appear instantaneously (**Fig.
297 3A**). Rather, active gels first display extensile dynamics before one or more asters nucleate (**Fig.
298 3A**). We systematically measured how aster density evolves with time and found that the aster
299 nucleation time increases when increasing the ATP concentration (**Fig. 3B**). Similarly, at the
300 microscopic scale, we observed that microtubules progressively gain their motor caps. We
301 measured that caps formed at a slower rate when ATP concentration is increased (**Fig. 3E**). To
302 compare these dynamics, we independently measured the time at which the first aster
303 nucleates in bulk samples and the time at which 10% of the microtubules have motor caps in
304 single microtubule assays using identical buffer conditions. Comparing the two characteristic
305 time scales showed that the dynamics of motor cap and aster formations are correlated (**Fig.
306 3F**). Taken together, these experiments confirmed that precise molecular regulation of the

binding, stepping, and unbinding of motor clusters onto microtubules at the microscopic scale controls both the dynamics and the final state of self-organization of the active gel at the macroscopic scale.

We are now able to better understand how adding passive PRC1 crosslinkers converts a contractile phase to an extensile phase (**Fig. S2D**). We hypothesize that the crosslinker promotes nematic alignment of the microtubules, while the motor cluster caps promote polar sorting and aster formation. We explored how other microscopic interactions that promote nematic alignment impact the emergent bulk dynamics. We assembled a globally contractile active crosslinked gel with PRC1 (**Fig. 4A)** and systematically increased microtubule bundling, crosslinking density, or nematic elasticity of the gel. Adding 2% (vol/vol) of 20kDa PEG favored extensile and aster formation over bulk contraction. It did not fully suppress contraction as small asters appeared after a few hours of extensile dynamics. (**Fig. 4B**). An extensive phase diagram for active gels with PEG suggests that the contractile-extensile phase boundary results from a competition between the ability to form polar motor caps and the depletion force (**Fig. 4J**). Further, adding passive semiflexible polymers in the background - either *fd* viruses [72], or DNA-origami rods [73] - also promotes nematic alignment of the microtubules [74] and triggers the contractile-to-extensile transition (**Fig. 4D, Fig S9**). Dual imaging at the single microtubule scale revealed that adding PEG, PRC1, or *fd* viruses did not prevent cap formation for isolated microtubules (**Fig. 4E-H**). The fact that two different semi-flexible polymers have the same effect on the transition argues that the impact of nematic alignment is generic (**Fig S9)**. Progressively increasing the nematic aligning interaction by adding more *fd* virus converts a globally contractile phase first into an aster phase, then into a fully extensile phase (**Fig. S10A-D**). The critical *fd* concentration that triggers the transition increases with motor cluster concentration (**Fig. S10E**).

Our results suggest that the extensile-contractile transition arises from the competing effects of microtubule end-clustering, which favors the formation of contractile asters, and factors promoting microtubule alignment, which favors the formation of extensile bundles (**Fig. 5A**). Based on this idea, we developed a simple model to rationalize the scaling behavior of this transition. We take a modeling approach akin to a self-assembly problem where polar and nematic interactions compete. Polar interactions depend on the ability of the motor clusters to end-accumulate and will lead to polarity-sorted contractile asters, while nematic interactions depend on the ability of the microtubules to stay aligned and will lead to extensile bundles. Using the well-known depletion interaction [75,76], we model the scaling of the effective strength of the alignment interaction between two microtubules as

(1) $V_{Alignment} = \alpha L[PEG]\rho^2$

where α is a proportionality constant, L is the average microtubule length, $[PEG]$ is the concentration of PEG in the system, and ρ is the number density of microtubules. The quadratic scaling for ρ results from the pair interaction between microtubules. Similarly, we model the effective strength of the end-adhesion interaction as

(2) $V_{end-adhesion} = \beta L \frac{[KSA_{ADP}]}{\rho}\rho^2 \; = \; \beta L[KSA_{ADP}]\rho$

where β is a proportionality constant and $\frac{[KSA_{ADP}]}{\rho}$ is the number of nonmotile, ADP-bound motor clusters per microtubule. In this model, the number of bound motors increases linearly with microtubule length, and thus the strength of end-adhesion interaction increases linearly with L. This scaling is motivated by the experimental observation that the probability of having a motor cap increases with microtubule length, which is reminiscent of an antenna model [58,67] (**Fig. S2E**). We considered that only ADP-bound motors that are attached at the end of a microtubule contribute to the end-adhesion. Considering an alternative model where ATP-bound motor clusters contribute to end-adhesion was incompatible with experimental measurements (**Supplementary Materials, section 5b**). We further assume that the binding of ATP to the motor clusters follows Michaelis-Menten kinetics, where the concentration of ADP-bound clusters is given by,

(3) $[KSA_{ADP}] = [KSA_{tot}](\frac{K_M}{K_M+[ATP]})$

where $[KSA_{tot}]$ is the total concentration of motor clusters, and K_M is the Michaelis constant for ATP binding to the motor clusters (aka the concentration of ATP where half of the motors are stepping).

In this framework, the phase boundary between the bundle and aster phases should lie when the nematic alignment interaction strength (**Eqn. 1**) equals polar end-adhesion interaction strength (**Eqn. 2**), providing a prediction for the phase boundary in the ATP-motor cluster plane.

(4) $[ATP] = \frac{\beta K_M}{\alpha\rho[PEG]}[KSA_{tot}] - K_M$

The experimental phase boundary separating the extensile bundle phase from the contractile aster phase in the ATP-motor cluster plane is linear in the range of concentrations explored (**Fig. 1K**), in qualitative agreement with the model. Fitting the experimental phase boundary to the model prediction (**Eqn. 4**), provides quantitative estimates of the model parameters $\frac{\beta K_M}{\alpha\rho[PEG]} = 376 \pm 147$ and $K_M = 14.5 \pm 25$ μM (fit values ± 95% confidence intervals).

We independently estimated $K_M = 78 \pm 41$ μM by measuring how the steady state speed of extensile gels varies with ATP concentration (**Fig. S11, Supplementary Materials, section 4c**), which is in agreement with reported values for the same K401 construct, albeit under different experimental conditions ($K_M = 96.4 \pm 25$ μM [77]). The difference between our two estimates might come from some oversimplification of the theory. Further work is needed to understand why the effective K_M derived from fitting the model differs from independent measurements.

Further, the model predicts that the phase boundary in the PEG-motor clusters phase diagram is linear, with a slope that can be determined from one of the previously measured fit parameters. We overlaid the fit-free prediction for the phase boundary with experimental data points and found excellent quantitative agreement between experiments and theory (**Fig. 4J**). Finally, the model offers additional predictions that qualitatively agree with the experimental data: the slope of the phase boundary i) scales inversely with the microtubule density (**Fig. S3A**); ii) is independent of microtubule density when PEG is replaced by PRC1 (**Fig. S3B, Supplementary Materials, section 5a)**.

In this framework, the emergent self-assembled structures are set by a single control parameter set by the ratio of K_M and the various component concentrations: $\frac{\rho[PEG]([ATP]+K_M)}{[KSA_{tot}]K_M}$. Estimating ρ from the known tubulin concentration, the number of protofilaments in a microtubule and the measured length distribution, we rescaled all the experimental data points from ~ 300 independent experiments, onto a single 1D phase diagram (**Fig. 5B**). We find that using this parameter, the data points segregate into three regions corresponding to the extensile, aster and globally contractile phases. The model predicts that the 1D phase boundary between the extensile and aster phase is set by the critical number density $\frac{\beta}{\alpha} = 41 +/- 15\ \mu M$ (95% confidence interval on linear fit). Below this critical density, the system is predicted to form asters, while above the system is predicted to form bundles. We next looked at the probability of being in a globally contractile, aster, or extensile phase as the ratio $\frac{\rho[PEG]([ATP]+K_M)}{[KSA_{tot}]K_M}$ increases (**Fig. 5C**). We find that the number density where extensile and contractile phases are equiprobable lies within the 95% confidence interval of the fitted value for $\frac{\beta}{\alpha}$ (**Fig. 5C**). The good agreement between theory and experiments suggests that the extensile-to-contractile transition can be described as a self-assembly process governed by the competition between polar and nematic alignment interactions (**Fig. 5A**).

Discussion:

Extensile and contractile stresses are ubiquitous in living and biomimetic active matter. Here, we bridged the length scale gap between the molecular interactions and the emergent macroscopic structure, explaining the transition from extensile bundles to contractile asters in active gels composed of stabilized microtubules and multivalent clusters of kinesin-1 motors. We identified salient molecular interactions that lead to either uniform motor distribution along microtubules and bulk extensile dynamics or the formation of motor caps and bulk contraction. Further, we showed that this symmetry breaking through end-clustering is not enough to fully explain the extensile-to-contractile transition. Nematic interactions driven by depletion or crosslinking can outcompete polar sorting to favor extensile bundles over polarity-sorted contractile asters. Based on these results, we formulated a simple self-assembly model based on the competition between polar interaction driven by end-accumulated motors and nematic alignment, and found quantitative agreement with the experimental data. We further verified predictions of the model and demonstrated that a single control parameter given by the ratio of the concentrations of the components sets the structural transition from extensile bundles to contractile asters.

It is unclear why this simple model captures the extensile-to-contractile transition so well (**Fig. 5C**). Indeed, this mean-field theory only considers pairwise interactions and lacks any higher-order cooperativity between microtubules, or between microtubules and motor clusters [78-80]. Second, this theory has no intrinsic timescales, hence no dependence on reaction rates which are crucial for explaining the interactions between kinesin and microtubules. Third, this model cannot describe the scale-dependent architecture of the active gels. When polar interactions dominate, microtubules with motor caps are predicted to form micelle-like structures with a radius of one microtubule length [10]. However, the aster sizes observed here

are orders of magnitude larger than a microtubule length, which clearly shows that the model cannot give information about the hierarchical organization that leads to the observed mesoscale structures (**Fig. 1I-J**). Consequently, this model does not describe the percolation transition from asters to globally contractile gels [81]. Finally, we expect that the critical ratio delineating the extensile and contractile phases will be different for different motors, cluster valency, or buffer conditions (**Fig. 5B, C**). One piece of evidence is that adding salt eliminates any contraction without changing the protein composition (**Fig. S7**) or that active gels driven by K365 and K401 kinesin-1 motor clusters respectively self-organize into bundles and asters despite having the same ATP and clusters concentrations.

These results further highlight that the design of the motor clusters is essential as the chemical kinetics between microtubules and the clusters, not just individual motor heads, dictates the self-organization of the active gel at the macroscale. Processivity is required to drive end-accumulation [58]. However, processivity of the clusters, and not necessarily of the individual motors themselves, is needed. We think light-activated K365 clusters cannot drive contraction because the clusters are non-processive by design (**Fig. S5A, Fig. S13**). In contrast, all the other constructs potentially form asters because the motor clusters are multivalent, hence highly processive, and can therefore end-accumulate (**Fig. S13)**.

Finally, the coexistence of contractile asters in an extensile gel is still not understood. Interestingly, we observed that only a fraction of microtubules break symmetry by forming a cap. Two populations of microtubules (with and without caps) coexisting at the single filament level might explain the coexistence of contractile asters and extensile bundles at the macroscopic scale. However, the physical or biochemical mechanisms for why only a fraction of microtubules forms caps are still unknown. This should be the focus of future work.

In thermodynamically driven self-assembly, molecular building blocks form an organized ordered structure that is set by the specific interaction rules between the various components. The diversity of possible structures is then a function of the diversity of the building blocks available. Self-organization in active matter is typically intractable because the emergent structures and dynamics are often a result of changing reaction rates rather than structural motifs and interactions. It is possibly one of the reasons why the cytoskeleton can self-organize into dramatically different structures using the same elementary building blocks. This work illustrates how to leverage simple concepts from self-assembly to understand complex emergent structures and dynamics in an out-of-equilibrium material powered by chemical reactions. Taken together, this work offers a blueprint to control pattern formation in biomimetic active matter, in particular for building multifunctional active materials that can be programmed into distinct or coexisting far-from-equilibrium structures.

Acknowledgment
We thank Shibani Dalal, director of the Brandeis Biomaterial Facility, for help with protein purification. B.N. thanks Saptorshi Ghosh for the discussion on data analysis. We thank Daichi Hayakawa for providing 6hb (helix bundle) DNA origami rods. We thank Linea Lemma for the opto-K365 constructs.

B.N. and G.D. acknowledge support from the NSF CAREER award DMR-2047119. P.J.F. and A.B. acknowledge support from the Brandeis NSF Materials Research Science and Engineering Center (MRSEC) DMR-2011846. We also acknowledge the use of the optical, microfluidics, and biomaterial facilities supported by NSF MRSEC DMR-2011846. A.B. acknowledges support from NSF-DMR-2202353.

Main Figures

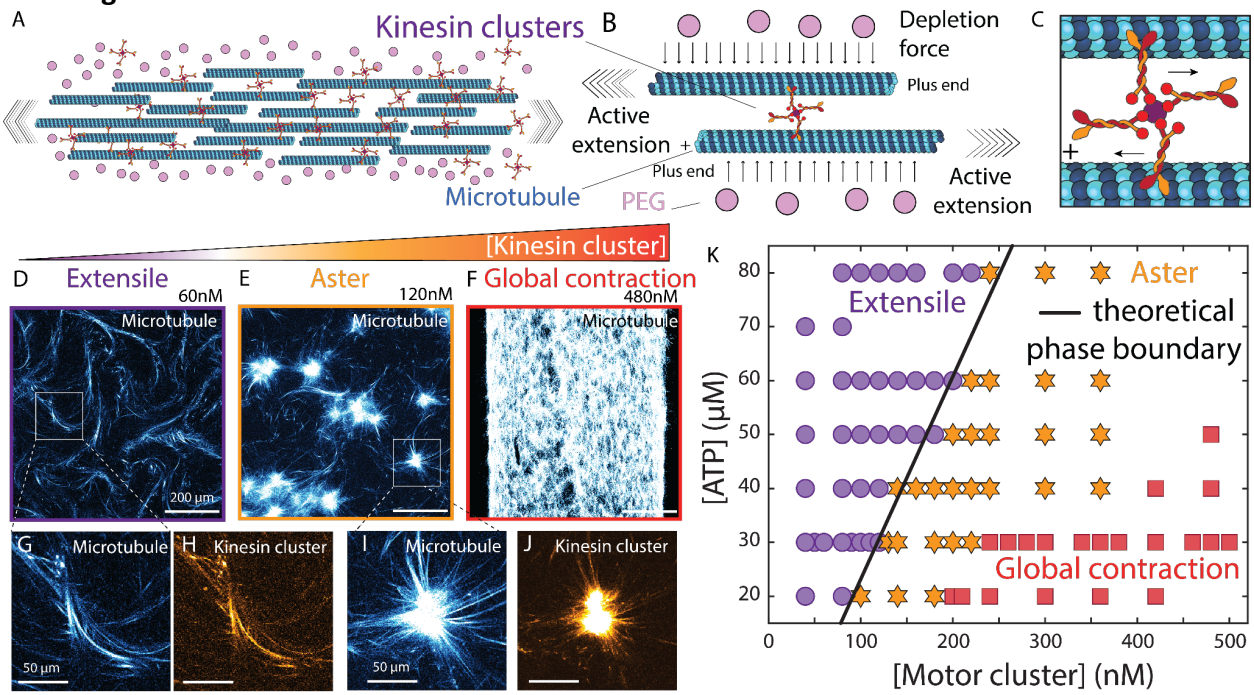

Figure 1: Multivalent clusters of Kinesin-1 molecular motor can drive microtubule gels into extensile, aster, or globally contractile phases. A) Schematic of an extensile bundle of stabilized microtubules. B) Close up on a pair of anti-parallel microtubules bundled by a non-specific depletant (PEG). C) Close up on the multivalent clusters of kinesin-1 motors. Motors are biotinylated and dimerize spontaneously. Clusters are formed by tetravalent streptavidin. Kinesin-1 motors walk toward the plus end of the microtubules. As a result, anti-parallel microtubules will slide apart when both are bound to a motor cluster. D) Fluorescent picture of the microtubule gel in the extensile phase ([motor clusters]=60nM). Increasing the cluster concentration first leads to the formation of E) an aster phase that locally contracts ([motor clusters]=120nM) and then F) a globally contractile phase ([motor clusters]=480nM). G and H respectively show close-ups of fluorescently labeled tubulin and motor clusters for an extensile bundle. I and J show close-ups of fluorescently labeled tubulin and motor clusters for an aster. K) ATP-motor cluster phase diagram: the critical concentration of motors needed to form asters and contract depends on the ATP concentration. Purple disks represent extensile bundles, orange stars are for asters, and red squares are for globally contractile gels. Each data point shown in K is an independent experiment. D-J were taken with a confocal microscope. Scale bars in D-F are 200 µm. Scale bars in G-J are 50 µm. In D-K, [ATP]= 30 µM, [tubulin]=1.33mg/mL.

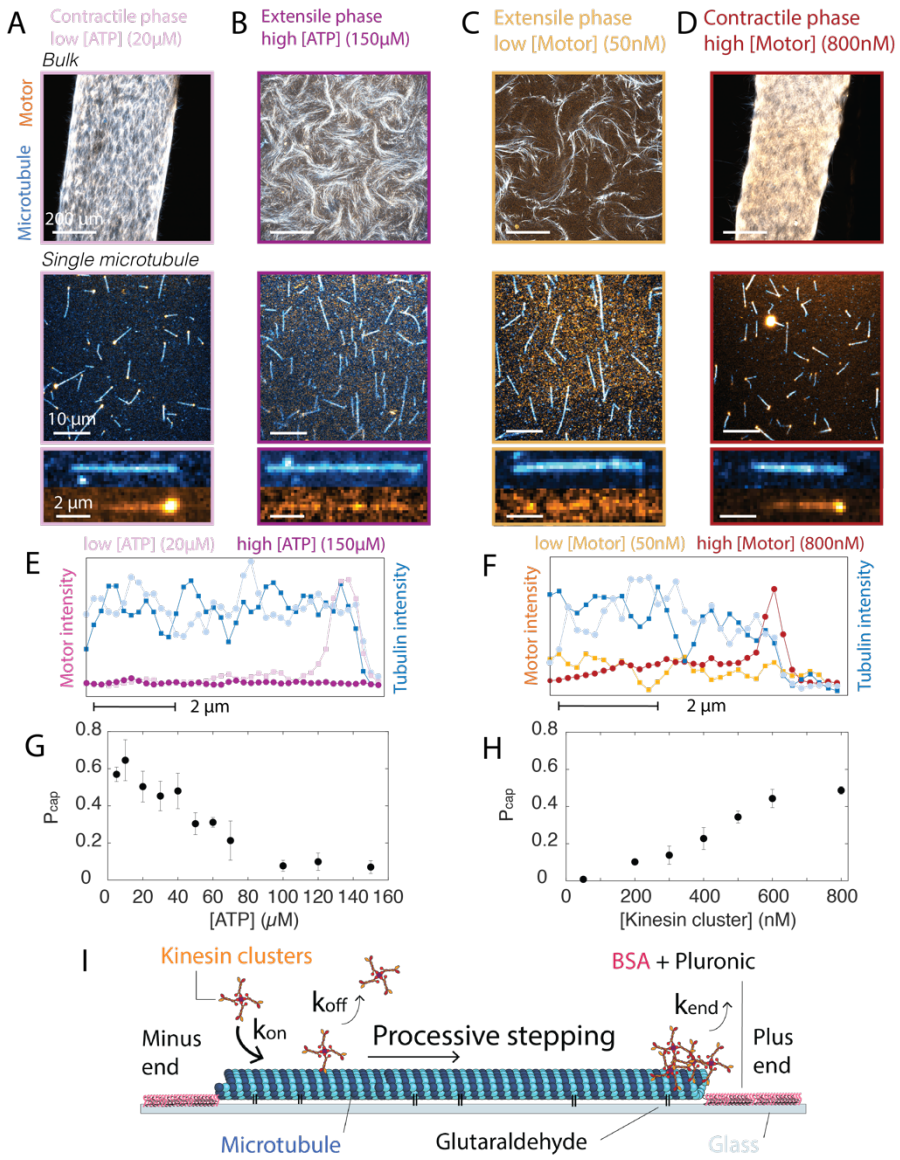

Figure 2: Kinetics of kinesin cluster-microtubule binding and unbinding can lead to motor cluster accumulation at the end of a microtubule. A-D) fluorescent pictures of bulk active gels and corresponding fluorescent pictures of isolated microtubules bound to a glass surface. Tubulin is labeled in cyan, motor clusters are in orange. Contraction and motor caps are detected both at A) low ATP concentration and D) high motor cluster concentration, while extensile dynamics and no caps were observed both at B) high ATP concentration or C) low motor cluster concentration. E and F show line scans of the fluorescent signal along a single microtubule for the pictures shown respectively in A-B and C-D. Microtubule profiles are in cyan, and motor cluster profiles are in magenta in E and orange in F. G) Fraction of microtubules with a motor cluster cap for increasing ATP concentrations. H) Fraction of microtubules with a motor cluster cap for increasing motor cluster concentrations. I) Schematic representation of the microscopic interaction between a microtubule and a kinesin-1 motor cluster. For A, B, E, and G [motor cluster]=480 nM; for C, D, F, and H, [ATP]=30 μM.

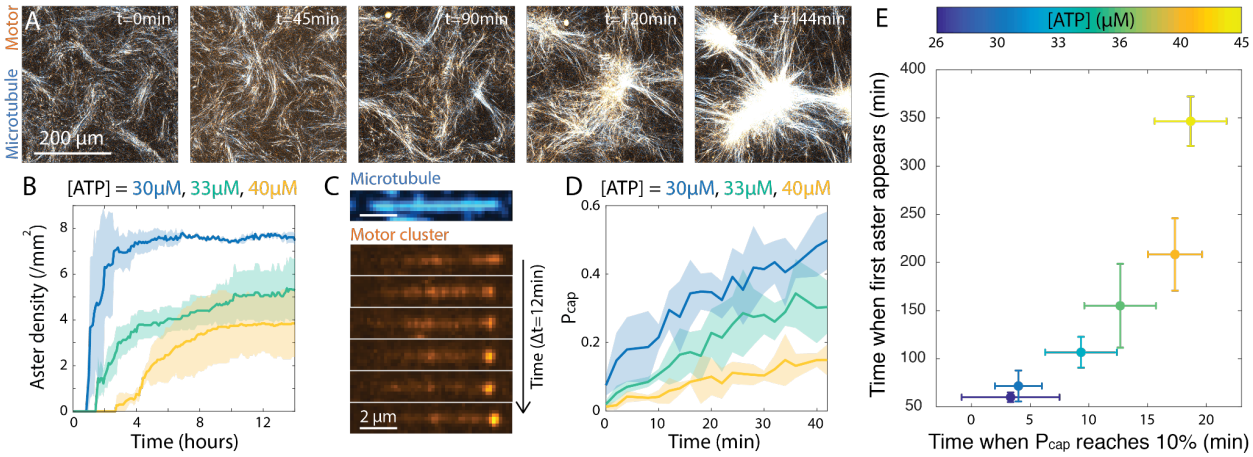

Figure 3: Dynamics of aster formation are correlated with the dynamics of motor cap formation. A) Time-series of the nucleation of an aster in an extensile active gel. Aster nucleates in an extensile background around 2h after the start of the experiment. Tubulin is labeled in cyan, motor clusters are in orange. [ATP]= 40µM, [motor cluster]=200nM, [PEG]=0.6% (vol/vol). B) Temporal evolution of the aster density for samples with increasing ATP concentrations. Asters appear faster with more ATP. C) Kymograph (space-time plot) of the formation of a motor cap at the end of a single microtubule. D) Temporal evolution of Pcap, the fraction of microtubules with a motor cap, for samples with increasing ATP concentrations. Motor caps appear faster with more ATP. F) Plot of the time when the first aster appears vs time when 10% of the microtubules gain a motor cap. Color code shows experiments at various ATP concentrations. A and C were taken with a confocal microscope. Scale bar in A is 200 µm. Each experiment in B, D, and F were repeated 3 times independently. Thick lines in B and D and disks in E show the mean, while shaded areas and errorbars show the standard deviation over the 3 replicates.

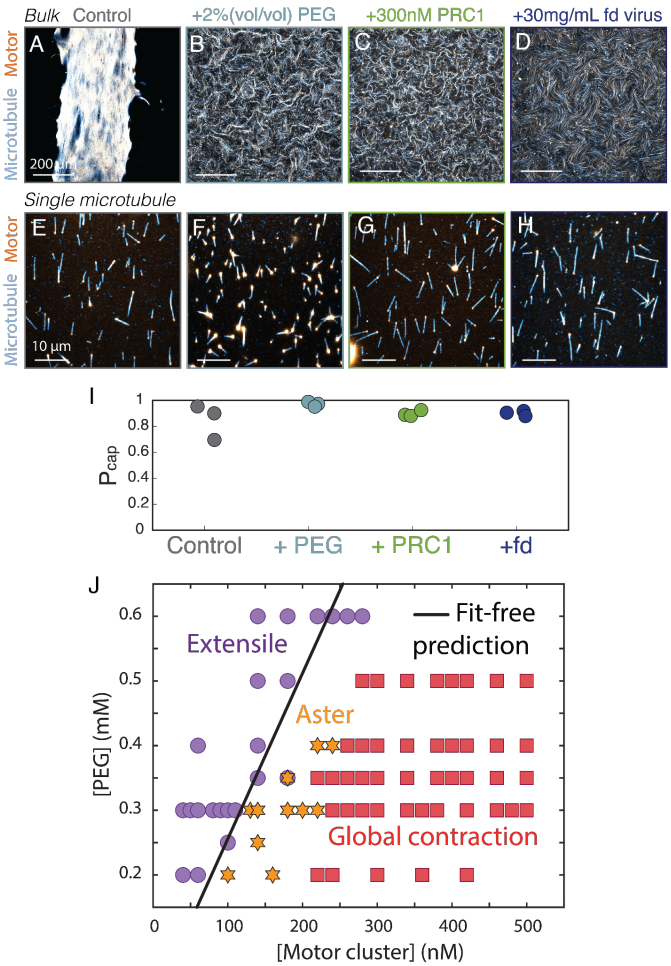

Figure 4: Nematic alignment outcompetes polar sorting to drive a contractile-to-extensile transition, despite the formation of motor caps at the single microtubule level. A) Fluorescent picture of an active crosslinked gel with PRC1 instead of PEG in the globally contractile phase ([ATP]=30µM, [Motor cluster]=480nM, [PRC1]=100nM, [MT]=1.33mg/mL). Tubulin is labeled in cyan, motor clusters are in orange. B) Adding 2% (vol/vol) of 20kDa PEG suppressed the global contraction and delayed the appearance of asters from an initially extensile phase by 3 hours. Adding C) 300nM of PRC1, or D) 30mg/mL of *fd* virus to increase nematic alignment fully suppresses any contraction over the lifetime of the sample (4 hours). Pictures in A-D were taken 1h after dynamics started. E-H) High-magnification microscopy of isolated microtubules for the same experimental conditions as A-D. Tubulin is labeled in cyan, motor clusters are in orange. I) Fractions of the microtubules with a motor cap for the same experimental conditions as A-D. each experiment was performed three times independently. J) PEG-Motor cluster phase diagram shows how the ratio of both components sets the extensile or contractile dynamics in active gels. Disks, stars, and squares represent the experimental data, while the black line represents the no-fit prediction derived from scaling arguments and the fitted parameters from the phase diagram in Fig. 1K. A-D were taken with a confocal microscope. Scale bar in A-D is 200 µm. Scale bar in E-H is 10 µm. Each data point shown in J comes from an independent experiment.

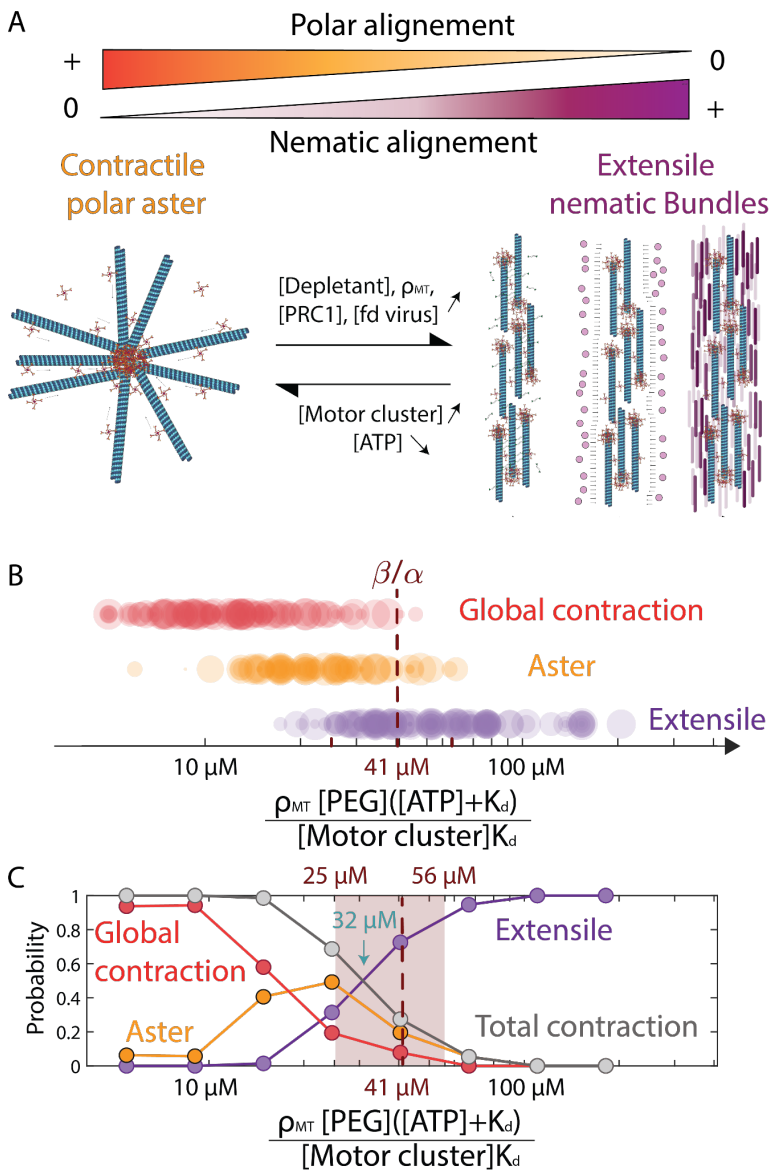

Figure 5: Nematic alignment competes with polar sorting to control the self-assembly into extensile bundles or contractile asters. A) Schematic representation of a contractile aster composed of polarity-sorted microtubules. Increasing the strength of nematic alignment by increasing the concentration of depletant, microtubule, PRC1 crosslinker, or *fd* virus can trigger a structural transition from aster to extensile bundles. Decreasing the concentration of motor cluster or increasing the concentration of ATP decreases the probability of cap formation, which decreases the strength of polar alignment interactions. At the macroscale, this leads to a transition from contractile asters to extensile bundles. B) Rescaled phase diagram that shows that all experimental data points collapse onto a single 1D line that only depends on K_d and the ratio of the components' concentrations. Original 2D phase diagrams are shown in **Fig. 1K, 4J,** and **S12**. The size of the semi-transparent disks is randomly assigned and the three phases are scattered along the y-axis to improve readability. C) Relative probability of finding the active gel in the extensile, aster, or globally contractile phases as the rescaled concentration increases. Above a critical microtubule density (C*=beta/alpha), the active gel evolves on average from a

contractile to extensile phase. The dashed line and the brown area respectively show the fitted value for C*=41µM and the corresponding interval of 95% confidence for C* [25-56µM] estimated from fitting the phase diagram in **Fig. 1K.** The experimental estimate of C* where extensile and contractile phases are equiprobable is 32µM. (In B-C, N=311 independent experiments, for [ATP]=20-150µM, [Motor cluster]=40-500nM, [PEG]=0.2-0.8mM, [MT]=2.7-16nM).

References

[1] M. C. Marchetti, J.-F. Joanny, S. Ramaswamy, T. B. Liverpool, J. Prost, M. Rao, and R. A. Simha, Reviews of Modern Physics **85**, 1143 (2013).

[2] W. B. Rogers, W. M. Shih, and V. N. Manoharan, Nature Reviews Materials **1** (2016).

[3] L. Wurthner, F. Brauns, G. Pawlik, J. Halatek, J. Kerssemakers, C. Dekker, and E. Frey, Proc Natl Acad Sci U S A **119**, e2206888119 (2022).

[4] D. Needleman and Z. Dogic, Nature Reviews Materials **2** (2017).

[5] H. Hess and J. L. Ross, Chem Soc Rev **46**, 5570 (2017).

[6] A. Bruce, A. Johnson, J. Lewis, M. Raff, K. Roberts, and P. Walter, *Molecular Biology of the Cell.* (Garland Science, New York, 2002), 4th edn.

[7] K.-T. Wu, J. B. Hishamunda, D. T. N. Chen, S. J. DeCamp, Y.-W. Chang, A. Fernández-Nieves, S. Fraden, and Z. Dogic, Science **355**, eaal1979 (2017).

[8] V. Schaller, C. Weber, C. Semmrich, E. Frey, and A. R. Bausch, Nature **467**, 73 (2010).

[9] B. Najma, M. Varghese, L. Tsidilkovski, L. Lemma, A. Baskaran, and G. Duclos, Nat Commun **13**, 6465 (2022).

[10] B. Lemma, N. P. Mitchell, R. Subramanian, D. J. Needleman, and Z. Dogic, Physical Review X **12** (2022).

[11] F. C. Keber, E. Loiseau, T. Sanchez, S. J. DeCamp, L. Giomi, M. J. Bowick, M. C. Marchetti, Z. Dogic, and A. R. Bausch, Science **345** (2014).

[12] K. L. Weirich, S. Banerjee, K. Dasbiswas, T. A. Witten, S. Vaikuntanathan, and M. L. Gardel, Proc Natl Acad Sci U S A **114**, 2131 (2017).

[13] L. Baldauf, L. van Buren, F. Fanalista, and G. H. Koenderink, ACS Synth Biol **11**, 3120 (2022).

[14] T. Sanchez, D. T. Chen, S. J. DeCamp, M. Heymann, and Z. Dogic, Nature **491**, 431 (2012).

[15] N. Kumar, R. Zhang, J. J. d. Pablo, and M. L. Gardel, Science Advances **7779** (2018).

[16] P. Chandrakar, M. Varghese, S. A. Aghvami, A. Baskaran, Z. Dogic, and G. Duclos, Phys Rev Lett **125**, 257801 (2020).

[17] F. J. Nedelec, T. Surrey, A. C. Maggs, and S. Leibler, Nature **389**, 305 (1997).

[18] F. Backouche, L. Haviv, D. Groswasser, and A. Bernheim-Groswasser, Phys Biol **3**, 264 (2006).

[19] D. Smith, F. Ziebert, D. Humphrey, C. Duggan, M. Steinbeck, W. Zimmermann, and J. Kas, Biophys J **93**, 4445 (2007).

[20] P. M. Bendix, G. H. Koenderink, D. Cuvelier, Z. Dogic, B. N. Koeleman, W. M. Brieher, C. M. Field, L. Mahadevan, and D. A. Weitz, Biophys J **94**, 3126 (2008).

[21] M. P. Murrell and M. L. Gardel, Proc Natl Acad Sci U S A **109**, 20820 (2012).

[22] P. J. Foster, S. Furthauer, M. J. Shelley, and D. J. Needleman, Elife **4** (2015).

[23] I. Linsmeier, S. Banerjee, P. W. Oakes, W. Jung, T. Kim, and M. P. Murrell, Nat Commun **7**, 12615 (2016).

[24] T. H. Tan, M. Malik-Garbi, E. Abu-Shah, J. Li, A. Sharma, F. C. MacKintosh, K. Keren, C. F. Schmidt, and N. Fakhri, Science Advances **2847** (2018).

[25] T. D. Ross, H. J. Lee, Z. Qu, R. A. Banks, R. Phillips, and M. Thomson, Nature **572**, 224 (2019).

[26] V. Wollrab, J. M. Belmonte, L. Baldauf, M. Leptin, F. Nedelec, and G. H. Koenderink, J Cell Sci **132** (2018).

[27] R. A. Banks, V. Galstyan, H. J. Lee, S. Hirokawa, A. Ierokomos, T. D. Ross, Z. Bryant, M. Thomson, and R. Phillips, bioRxiv (2022).

[28] J. Berezney, B. L. Goode, S. Fraden, and Z. Dogic, Proc Natl Acad Sci U S A **119** (2022).

[29] N. Kumar, R. Zhang, J. J. d. Pablo, and M. L. Gardel, Science Advances **4** (2018).
[30] R. Zhang *et al.*, Nat Mater **20**, 875 (2021).
[31] T. Gao, R. Blackwell, M. A. Glaser, M. D. Betterton, and M. J. Shelley, Phys. Rev. Lett. **114**, 048101 (2015).
[32] A. Lamtyugina, Y. Qiu, E. Fodor, A. R. Dinner, and S. Vaikuntanathan, Phys Rev Lett **129**, 128002 (2022).
[33] R. Blackwell, O. Sweezy-Schindler, C. Baldwin, L. E. Hough, M. A. Glaser, and M. D. Betterton, Soft Matter **12**, 2676 (2016).
[34] K. Kruse and F. Jülicher, Phys. Rev. Lett. **85** (2000).
[35] J. M. Belmonte, M. Leptin, and F. Nedelec, Mol Syst Biol **13**, 941 (2017).
[36] M. Lenz, Physical Review X **4** (2014).
[37] S. Stam, S. L. Freedman, S. Banerjee, K. L. Weirich, A. R. Dinner, and M. L. Gardel, Proc Natl Acad Sci U S A **114**, E10037 (2017).
[38] D. V. Koster, K. Husain, E. Iljazi, A. Bhat, P. Bieling, R. D. Mullins, M. Rao, and S. Mayor, Proc Natl Acad Sci U S A **113**, E1645 (2016).
[39] P. J. Foster, S. Fürthauer, and N. Fakhri, bioRxiv (2022).
[40] J. Brugues and D. Needleman, Proc Natl Acad Sci U S A **111**, 18496 (2014).
[41] D. Oriola, D. J. Needleman, and J. Brugues, Annual Review of Biophysics **47** (2018).
[42] J. Roostalu, J. Rickman, C. Thomas, F. Nedelec, and T. Surrey, Cell **175**, 796 (2018).
[43] G. Henkin, W. X. Chew, F. Nedelec, and T. Surrey, Proc Natl Acad Sci U S A **119**, e2206398119 (2022).
[44] G. Sarfati, A. Maitra, R. Voituriez, J. C. Galas, and A. Estevez-Torres, Soft Matter **18**, 3793 (2022).
[45] P. Ronceray, C. P. Broedersz, and M. Lenz, Proc Natl Acad Sci U S A **113**, 2827 (2016).
[46] G. Henkin, S. J. DeCamp, D. T. Chen, T. Sanchez, and Z. Dogic, Philosophical Transactions of the Royal Society A: Mathematical, Physical and Engineering Sciences **372**, 20140142 (2014).
[47] T. Surrey, F. Nédélec, S. Leibler, and E. Karsenti, Science **292** (2001).
[48] F. Verde, J. M. Berrez, C. Antony, and E. Karsenti, Journal of Cell Biology **112**, 1177 (1991).
[49] K. E. Sawin, K. LeGuellec, M. Philippe, and T. J. Mitchison, Nature **359**, 540 (1992).
[50] T. Gaglio, A. Saredi, and D. A. Compton, Journal of Cell Biology **131**, 693 (1995).
[51] S. Ramaswamy, Nature Reviews Physics **1**, 640 (2019).
[52] P. J. Foster, S. Fürthauer, M. J. Shelley, and D. J. Needleman, Current Opinion in Cell Biology **56**, 109 (2019).
[53] R. A. Simha and S. Ramaswamy, Phys. Rev. Lett. **89**, 058101 (2002).
[54] B. Martínez-Prat, R. Alert, F. Meng, J. Ignés-Mullol, J.-F. Joanny, J. Casademunt, R. Golestanian, and F. Sagués, Physical Review X **11** (2021).
[55] J. Prost, F. Jülicher, and J. F. Joanny, Nature Physics **11**, 111 (2015).
[56] K. Nishinari, Y. Okada, A. Schadschneider, and D. Chowdhury, Phys Rev Lett **95**, 118101 (2005).
[57] V. Varga, J. Helenius, K. Tanaka, A. A. Hyman, T. U. Tanaka, and J. Howard, Nat Cell Biol **8**, 957 (2006).
[58] C. Leduc, K. Padberg-Gehle, V. Varga, D. Helbing, S. Diez, and J. Howard, Proc Natl Acad Sci U S A **109**, 6100 (2012).
[59] R. Tan, P. J. Foster, D. J. Needleman, and R. J. McKenney, Developmental Cell **44**, 233 (2018).
[60] D. A. Gagnon, C. Dessi, J. P. Berezney, R. Boros, D. T. N. Chen, Z. Dogic, and D. L. Blair, Phys. Rev. Lett. **125** (2020).
[61] M. Lenz, Elife **9** (2020).
[62] F. e. Benoist, G. Saggiorato, and M. Lenz, arXiv preprint arXiv:2206.04444 (2022).

[63] R. Subramanian, E. M. Wilson-Kubalek, C. P. Arthur, M. J. Bick, E. A. Campbell, S. A. Darst, R. A. Milligan, and T. M. Kapoor, Cell **142**, 433 (2010).
[64] P. Bieling, I. A. Telley, and T. Surrey, Cell **142**, 420 (2010).
[65] P. Chandrakar *et al.*, Soft Matter **18**, 1825 (2022).
[66] S. Fürthauer, D. J. Needleman, and M. J. Shelley, New Journal of Physics **23**, 013012 (2021).
[67] L. Mohapatra, B. L. Goode, P. Jelenkovic, R. Phillips, and J. Kondev, Annual Review of Biophysics **45**, 85 (2016).
[68] K. Furuta, A. Furuta, Y. Y. Toyoshima, M. Amino, K. Oiwa, and H. Kojima, Proc Natl Acad Sci U S A **110**, 501 (2013).
[69] W. O. Hancock and J. Howard, Proceedings of the National Academy of Sciences **96**, 13147 (1999).
[70] L. M. Lemma, M. Varghese, T. D. Ross, M. Thomson, A. Baskaran, and Z. Dogic, arXiv preprint arXiv:2209.06277v1 (2022).
[71] G. Guntas, R. A. Hallett, S. P. Zimmerman, T. Williams, H. Yumerefendi, J. E. Bear, and B. Kuhlman, Proc Natl Acad Sci U S A **112**, 112 (2015).
[72] Z. Dogic and S. Fraden, Langmuir **16**, 7820 (2000).
[73] M. Siavashpouri, C. H. Wachauf, M. J. Zakhary, F. Praetorius, H. Dietz, and Z. Dogic, Nature Materials **16**, 849 (2017).
[74] G. Duclos *et al.*, Science **367**, 1120 (2020).
[75] S. Asakura and F. Oosawa, The Journal of Chemical Physics **22**, 1255 (1954).
[76] B. Götzelmann, R. Evans, and S. Dietrich, Physical Review E **57**, 6785 (1998).
[77] K. M. Brendza, D. J. Rose, S. P. Gilbert, and W. M. Saxton, J Biol Chem **274**, 31506 (1999).
[78] A. Vilfan, E. Frey, F. Schwabl, M. Thormählen, Y. H. Song, and E. Mandelkow, J Mol Biol **312**, 1011 (2001).
[79] W. H Roos, O. Campàs, F. Montel, G. Woehlke, J. P. Spatz, P. Bassereau, and G. Cappello, Physical Biology **5**, 046004 (2008).
[80] S. S. Wijeratne, S. A. Fiorenza, A. E. Neary, R. Subramanian, and M. D. Betterton, Proc Natl Acad Sci U S A **119**, e2120193119 (2022).
[81] J. Alvarado, M. Sheinman, A. Sharma, F. C. MacKintosh, and G. H. Koenderink, Nature Physics **9**, 591 (2013).

Methods and Materials

Title: Microscopic interactions control a structural transition in active mixtures of microtubules and molecular motors

Author list:
Bibi Najma[1], Aparna Baskaran[1], Peter J. Foster[1,2], Guillaume Duclos[1,*]

Affiliations:
[1]Department of Physics, Brandeis University, Waltham, MA 02453
[2]Present address: Department of Physics and Astronomy, University of Southern California, Los Angeles, CA, 90089, USA
[*]gduclos@brandeis.edu

1. Protein purification protocols

Microtubules

Tubulin dimers were purified from bovine brains through two cycles of polymerization–depolymerization in high molarity PIPES (1,4-piperazindiethanesulfonic acid) buffer [1]. Fluorophore-labeled tubulin was prepared by labeling the purified tubulin with Alexa-Fluor 647-NHS (Invitrogen, A-20006) [2]. GMPCPP (Guanosine 5'-(α,β, methylenetriphosphate)), a non-hydrolyzable analog of GTP, was used to stabilize the dynamic instability in the MTs. The polymerization mixture consisted of 80 µM tubulin (with 3% fluorescently labeled tubulin), 0.6 mM GMPCPP, and 1 mM dithiothreitol (DTT) in M2B buffer (80 mM PIPES, 1 mM EGTA, 2 mM MgCl2). After adding all the components, the mixture was incubated at 37 °C for 30 min, and subsequently for 6 h at room temperature (25 °C). This method resulted in MTs of 1.5 µm length [3]. The stock concentration was 8 mg/mL of tubulin. MTs were aliquoted in small volumes (5 µL), flash-frozen in liquid nitrogen, and stored at −80 °C.

Crosslinkers—PRC1-NSΔC

The truncated PRC1-NSΔC (MW: 58 kDa), a microtubule crosslinking protein, was expressed and purified in Rosetta BL21(DE3) cells using an established protocol described elsewhere [4,5]. The proteins were flash-frozen with 40% sucrose and stored at −80 °C. The final concentration of PRC1 was measured by a Bradford assay.

Molecular motors—K401 and K365 motors

K401-BIO-6xHIS (processive motor, dimeric MW: 110 kDa) and K365-BIO-6xHIS (non-processive motor, MW: 50 kDa) are biotinylated kinesin constructs derived from N-terminal domain of Drosophila melanogaster kinesin-1, truncated at residue 401 and 365, respectively, and labeled with six histidine tags. The motor proteins were transformed and expressed in Rosetta (DE3) pLysS cells and purified following established protocols described previously [6]. The proteins were stored in a 40% w/vol sucrose solution at −80 °C. The final concentration of kinesin was measured by Bradford assay.

We used tetrameric streptavidin (ThermoFisher, 21122, MW: 52.8 kDa) to assemble clusters of biotinylated kinesins (KSA). To make K401-streptavidin clusters, 5.7 µL of 6.6 µM streptavidin was mixed with 5 µL of 6.4 µM K401 and 0.5 µL of 5 mM DTT in M2B. This mixture was incubated on ice for 30 minutes. K365-streptavidin clusters were prepared by mixing 5.7 µL of 6.6 µM streptavidin, 3.1 µL of 20 µM K365, 0.5 µL of 5 mM DTT, and 1.94 µL of M2B and then left to incubate on ice for 30 min.

Light-activable motors: K365-iLID and K365-micro

K365-iLID and K365-micro were designed by Linnea Lemma and Tyler Ross and were purified following the protocol described in ref. [7,8]. Briefly, two chimeras of the D. melanogaster kinesin K365, namely, K365-iLID and K365-micro, were expressed in Escherichia coli Rosetta 2(DE3)pLysS cells and purified using ÄKTA pure FPLC system. MBP domain was cleaved with TEV protease (Sigma Aldrich). The proteins were snap-frozen in 40% glycerol and stored at −80 °C.

2. Assembling 3D active gels for bulk experiments

The active gels are composed of:

- Alexa 647-labeled GMPCPP stabilized MTs with an exponential distribution of lengths with an average of 1.5 µm, unless otherwise specified,
- Multi-motor kinesin complexes self-assembled from tetrameric streptavidin and two-headed biotinylated kinesin (K401-Bio) or single-headed biotinylated kinesin (K365-Bio)
- MT bundling, (0.6-2)% (w/v) PEG (polyethylene glycol, 20 kDa, Sigma) or 100nM PRC1, that passively crosslink antiparallel MTs, but still allow interfilament sliding,
- ATP (Sigma)
- An ATP regeneration system: phosphoenol pyruvate (53 mM PEP, Beantown Chemical, 129745) and pyruvate kinase/lactate dehydrogenase enzymes (2.8% v/v PK/LDH, Sigma, P-0294). For experiments with PRC1, we used 26mM of PEP.
- An oxygen scavenging system comprised of glucose (18.7 mM), DTT (5.5 mM), glucose oxidase (1.4 µM), and catalase (0.17 µM) was used to decrease photobleaching.

For consistency, a large volume of premix was prepared, aliquoted, and snap-frozen in liquid nitrogen for each phase diagram (Fig. 1 & Fig. 4) . Frozen MTs (stored at −80 °C) were thawed immediately before use in an experiment. All the experiments were performed at room temperature. Active networks composed of MTs (1.3 mg/mL), ATP (1420 µM), and K401 clusters (120 nM) remain active for 6–8 h.

2.a Flow chamber assembly for bulk experiments

All flow chambers have the same dimensions (H = 80 µm, W = 3 mm) and were assembled using two glass slides spaced by a layer of parafilm. The glass surfaces were coated with an acrylamide brush to resist non-specific protein adsorption [2]. Parafilm spacers were cut and placed between the two glass surfaces followed by a mild heat treatment at 60 °C to melt parafilm so it can bind to the glass surfaces. The active mixture was loaded into each channel type by capillarity and sealed with an UV-curing optical adhesive (NOA 81, Norland Products Inc.).

2.b Flow chambers for single microtubule studies

The flow chambers were constructed as previously described [9]. In brief, we built a chamber by assembling two silanized coverslips (VWR, Germany) on the glass spacers cut out of a coverslip (thickness ≈ 0.140 mm). The chamber was incubated with 16% (v/v) glutaraldehyde (Electron Microscopy Sciences) for 30 minutes. For single molecule studies, the MTs were polymerized from a solution of 80 µM of 20% Alexa647- labeled tubulin. Microtubules (115 nM tubulin) were incubated in the flow chamber at room temperature. The remaining exposed surface was blocked for 5 minutes with 6% Pluronic F-127 (w/v) (Sigma P2443. MW: 12.5 kDa) and 15mg/ml of Bovine Serum Albumin (BSA, Sigma) solution.

The imaging buffer consisted of M2B supplemented with 4 mg/ml BSA, (0-2)% (w/v) PEG (polyethylene glycol, 20 kDa), 3mM MgCl2, ATP (ranging from 5 to 200 µM), ATP regeneration system, 2mM Trolox, an oxygen scavenging system, and motor clusters ranging from 40 to 800 nM (Alexa 568 or Alexa 488 labeled Streptavidin).

3. Microscopy

Widefield microscopy

The Alexa 647-labeled MT networks were imaged using an inverted wide-field microscope (Nikon Ti-E or Ti2) with a fluorescent filter (Semrock Cy5-4040C), a SOLA light engine (Lumencor), 10x (Nikon Pan Fluor, NA 0.3) or 4x objective (Nikon Pan Fluor, NA 0.13) and a CCD or a sCMOS camera (Andor Clara E, Hamamatsu orca flash 4.0). The illumination and the data

acquisition were controlled by micro-manager (µManager, Version 2.0.0-gamma [10]). All the measurements were performed at room temperature.

Confocal microscopy

Imaging of motor cluster transport and accumulation on microtubule plus ends was performed using Leica Application Suite X (LAS X) control on a laser scanning confocal microscope (TCS-SP8, Leica Microsystems GmbH) equipped with photomultiplier tubes.

For excitation, 638 nm laser diode for Alexa Fluor 647 labeled microtubules, 488 nm or 552 nm laser diodes for Alexa Fluor 488 or Alexa Fluor 568-labeled motor clusters, respectively. Images were acquired using an oil-immersion 63x objective (HCX PL Fluotar, NA =1.4).

4. Image and Data Analysis

4.a Single filament cap analyses

The probability distribution of motor caps at microtubule ends was measured using a custom-written MATLAB program. We collected timelapse series of dual-channel confocal images where both tubulin and motor clusters were labeled. In brief, we first segmented microtubules after excluding microtubules at the edges of the image. The motor channel was scanned along the length of each segmented microtubule for the presence of a motor cap by comparing the maximum intensity to the average intensity of the background. If that ratio was greater than 2.5, then a cap was detected. The probability distribution of caps is calculated by taking the ratio of the number of caps to the number of microtubules for each image and plotted as a function of time. The run lengths of the motor clusters (Fig. S2 and S3) were determined from the kymographs using the reslice tool in Fiji (National Institutes of Health) [11].

4.b How to determine if the system is in the extensile/contractile/ or globally contractile state?

Time series of samples with fluorescent microtubules were inspected by eye. Asters are identified as local and sustained densification of the microtubules. In the absence of contraction over the entire lifetime of the sample (10-12h), the dynamics are labeled as extensile. If any asters form during the lifetime of the sample, the gel is labeled as an aster phase.

4.c Determination of K_M

We measured K_M by quantifying the ATP dependence of active flow speeds. We measured the average speed of active flows as a function of ATP over three decades of ATP concentration. The average speed vs. ATP data were well fitted by Michaelis–Menten kinetics (Fig.S11).

Premixes of extensile gels were prepared with different ATP concentrations between 20 and 1420 µM using 110 nM Motor clusters and 1.33mg/mL of tubulin. For each ATP concentration, the experiment was repeated four independent times.

Flow fields of microtubule bundles were measured using MATLAB-based open-source particle image velocimetry (PIV) [12]. An interrogation window size of 64 pixels = 82.56µm was selected with 50% overlap. The average speed vs. ATP data were well fitted by Michaelis–Menten kinetics (**Fig.S11**).

4.d Estimation of the microtubules number density

For a microtubule of 1.5µm length, there are about 13 protofilaments, hence 2440 tubulin dimers. If one tubulin dimer weighs 100 kDa then one microtubule weighs 244,000 kDa. Therefore, for an active network containing 1.33mg/mL of tubulin, the microtubule number density is 5.45nM (if one considers that all the tubulin will polymerize into microtubules).

5. Theoretical model

5.a Model for PRC1-based active gels

When PEG was replaced by a microtubule-specific crosslinker PRC1, the effective strength of the alignment interaction changed in the following way:

(1) $V_{Alignment} = \alpha L \frac{[PRC1]}{\rho} \rho^2$

Where α is a proportionality constant, L is the average microtubule length, ρ is the number density of microtubules, and $\frac{[PRC1]}{\rho}$ is the number of PRC1 per microtubule. The effective strength of end-adhesion alignment is the same as in the main text:

(2) $V_{end-adhesion} = \beta L \frac{[KSA_{ADP}]}{\rho} \rho^2 = \beta L [KSA_{ADP}] \rho$

where β is a proportionality constant and $\frac{[KSA_{ADP}]}{\rho}$ is the number of nonmotile, ADP-bound KSA per microtubule.

We end up with the following equation for the phase boundary:

(3) $[ATP] = \frac{\beta K_M}{\alpha [PRC1]} [KSA_{tot}] - K_M.$

This model predicts that the slope of the phase boundary is independent of microtubule density for PRC1-based active gels.

5.b Model for ATP-bound motor clusters

We tried to estimate how the extensile/contractile phase boundary would look like if we considered only the ATP-bound motor clusters.

(4) $[KSA_{ATP}] = [KSA_{tot}] (\frac{[ATP]}{K_M + [ATP]})$

We ended up with the following equation for the phase boundary:

(5) $$[ATP] = \frac{K_M}{\frac{\beta}{\alpha[PEG]\rho}[KSA_{tot}] - 1}$$

This phase boundary does not agree at all with the experimental data (**Fig. 1K**), suggesting that we should consider the ADP-bound motors as contributing to the end-clustering, not the ATP-bound motors.

6. Supplementary figures

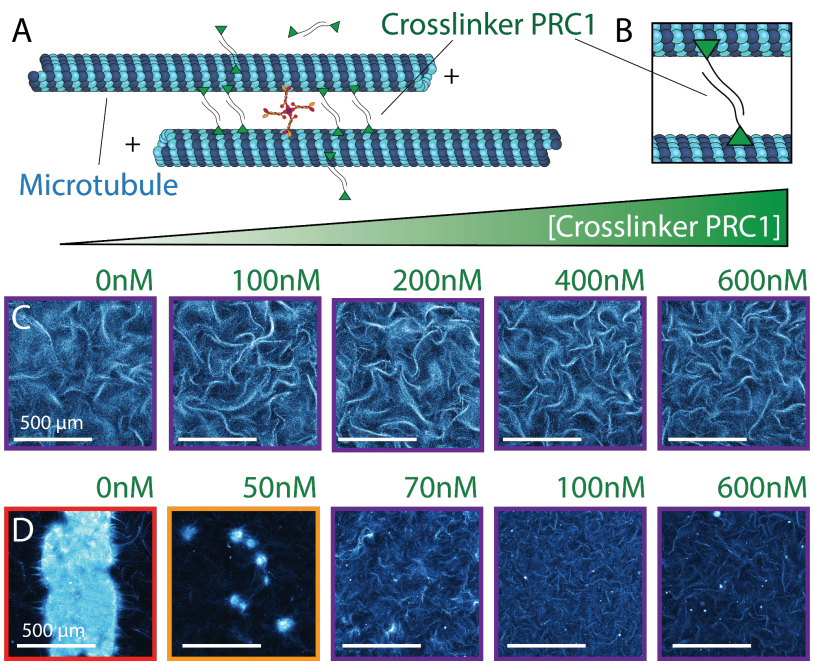

Figure S1: Extensile to contractile transition is not controlled by the ability of motor clusters to crosslink microtubules in the absence of ATP. A) Schematic of a microtubule bundle crosslinked by PRC1. B) Close up on a PRC1 dimer crosslinking two anti-parallel microtubules. C) Fluorescent pictures of an extensile phase with increasing concentrations of crosslinker (from 0 to 600nM). Adding an increasing amount of crosslinkers does not impact the extensile nature of the active gel. [ATP]=30µM, [motor cluster]=100nM. D) Fluorescent pictures of a globally contractile phase with increasing concentrations of crosslinker (from 0 to 600nM). Adding an increasing amount of crosslinkers progressively transforms a globally contractile phase into an extensile phase. D-E were taken with a confocal microscope. Scale bars in G-J are 500 µm. [ATP]=30 µM, [motor cluster]=480nM.

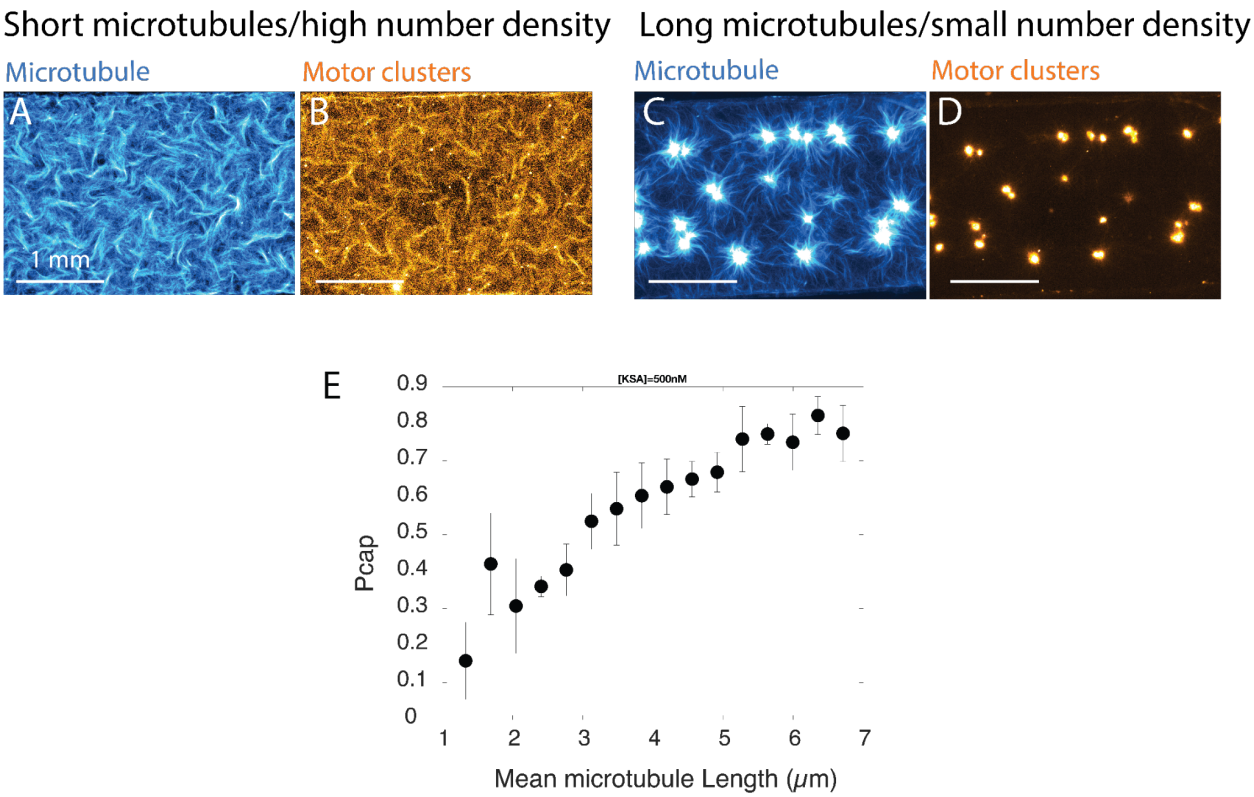

Figure S2: Increasing the microtubule's average length while keeping tubulin concentration constant leads to a transition from extensile to contractile dynamics. Fluorescent images of tubulin and motor clusters for an average microtubule length of A-B) 2.7um and C-D) 6.0um and a tubulin concentration of 1.33mg/mL. E) fraction of microtubule with a motor cap as a function of the microtubule length. Longer microtubules have a higher probability of forming a motor cap. [Motor cluster]=110nM, [ATP]=30µM. Error bars show standard deviation over binned microtubule of length mean+/-0.5µm. Data shown in E comes from 18 experimental conditions where ATP and motor cluster concentrations were varied over [ATP]=5-150µM and [Motor cluster]=50-800nM. Each experimental condition was repeated 3 times.

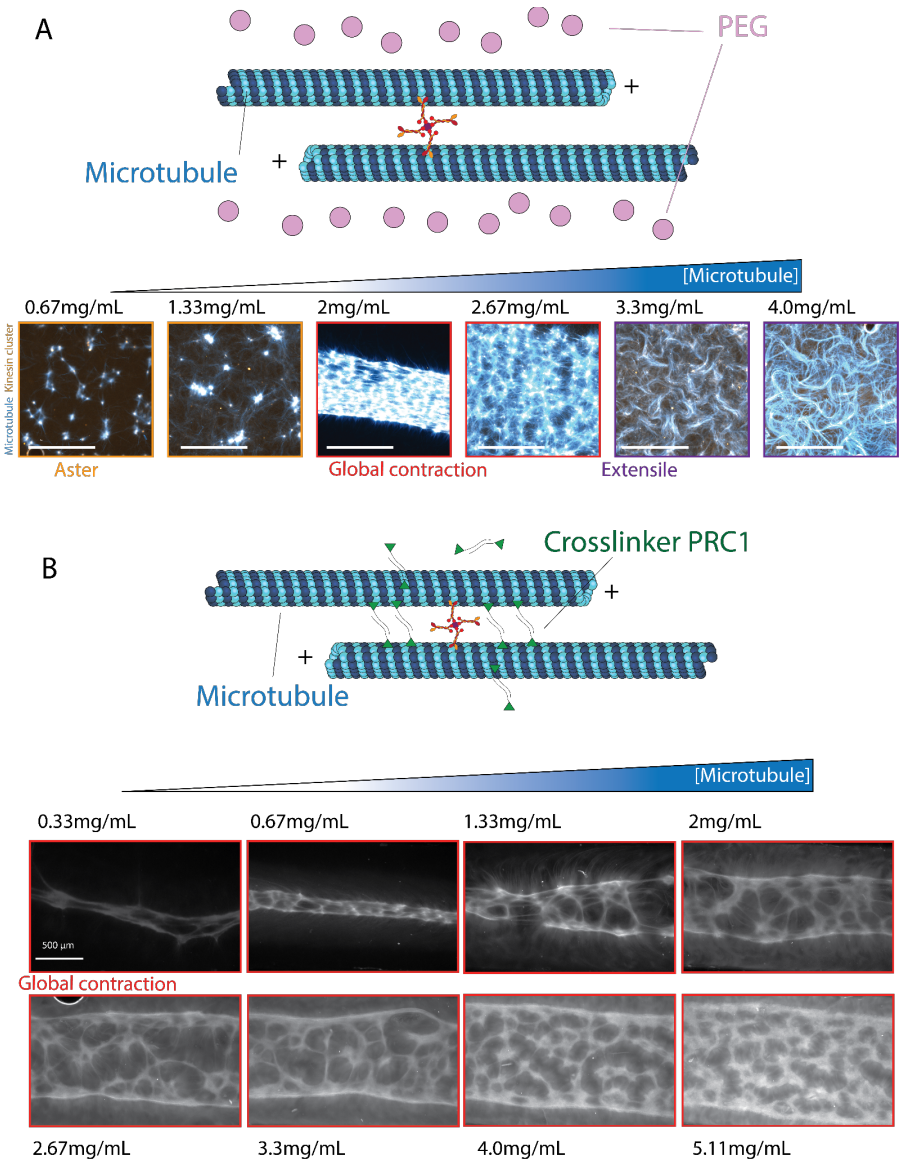

Figure S3: Increasing microtubule concentration leads to a contractile-to-extensile transition for PEG-based active gel and does not impact the dynamics of PRC1-based active gels. A) schematic of a PEG-based bundle and fluorescent images of tubulin (cyan) and motor cluster (orange) when tubulin concentration is increased while keeping the average microtubule length constant. Scale bar is 1 mm, Images were taken with a confocal microscope. [ATP]=30µM, [Motor cluster]=200nM, [PEG-20kDa]=0.6% (vol/vol). B) schematic of a PRC1-based bundle and fluorescent images of microtubules when tubulin concentration is increased. [ATP]=30µM, [Motor cluster]=380nM, [PRC1]=100nM.

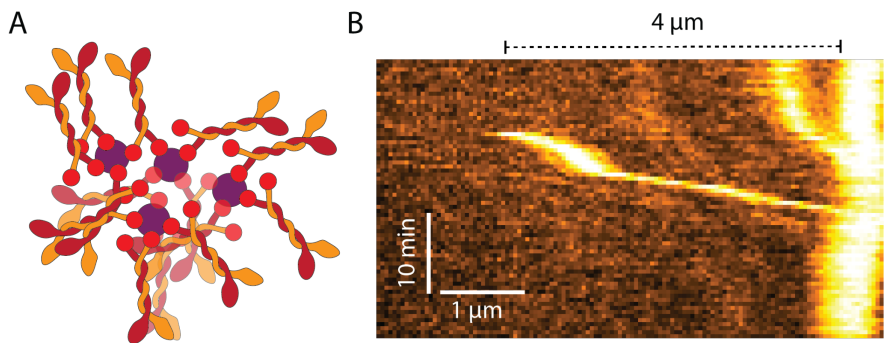

Figure S4: High processivity of clusters of dimeric K401 kinesin-1. A) Hypothesized structure of clusters of biotin-K401 and streptavidin. The exact valency of the motor clusters is unknown because motors can spontaneously dimerize, offering 2 biotin binding sites per dimer. B) Kymograph (space-time plot) showing a labeled motor cluster binding and moving onto a microtubule. The run length is longer than 4µm. The motor cluster reaches the dense motor cap at the end of the microtubule.

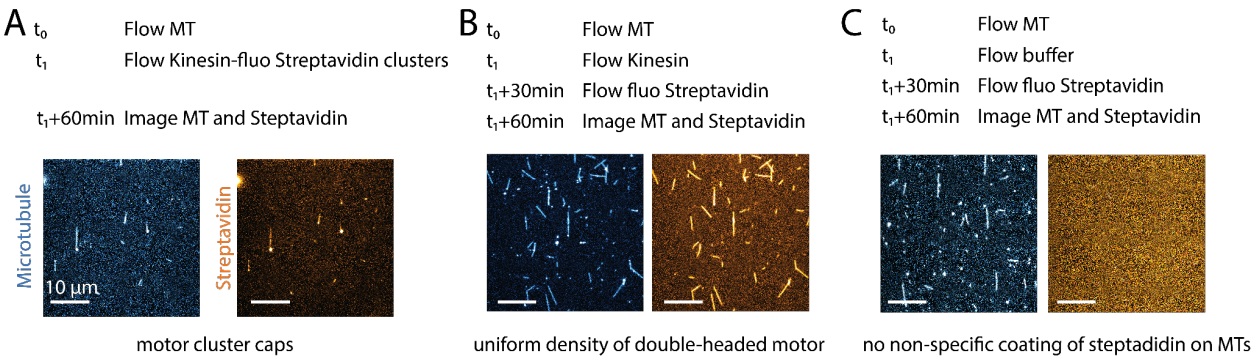

Figure S5: Motor caps form when kinesin motors are clustered by Streptavidin. A) single microtubule pictures where caps are formed when clusters of kinesin-Streptavidin are added to MTs. B) When kinesin-1 and Streptavidin are flown sequentially, no caps are observed. C) in the absence of Kinesin, Streptavidin does not bind to microtubules. Tubulin is labeled in cyan, and Streptavidin is in orange. Scale bars are 10 µm.

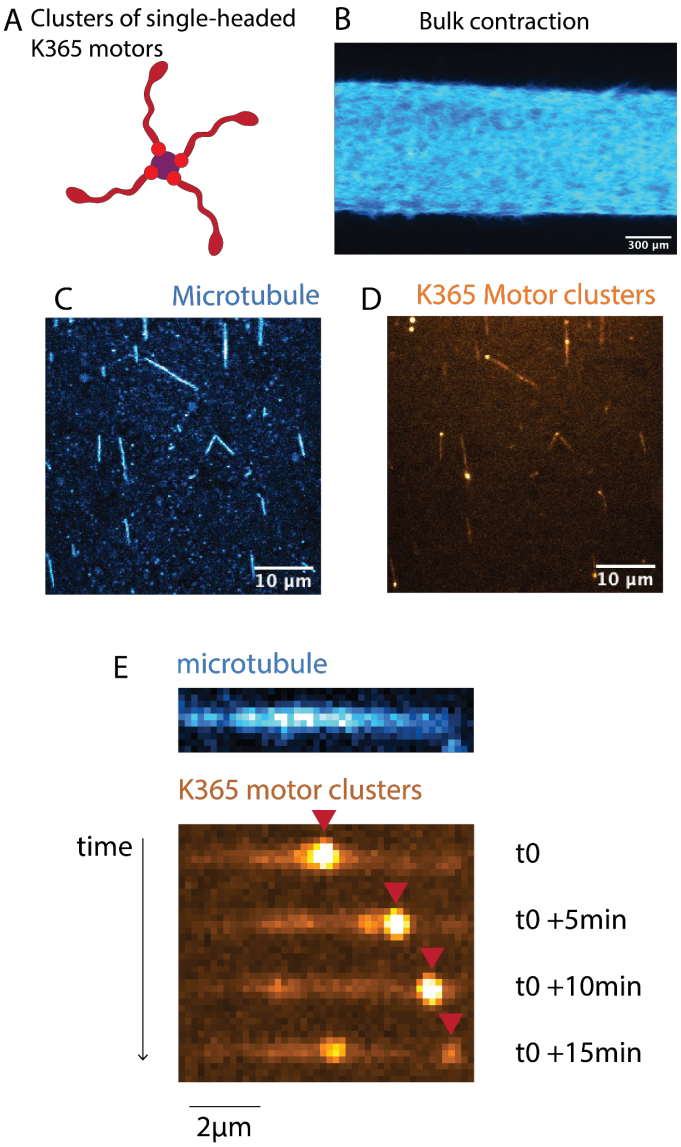

Figure S6: Contraction and end-accumulation clusters of monomeric K365 kinesin-1 onto microtubules. A) Schematic of a motor cluster. Contrary to K401, K365 does not spontaneously dimerize, which should lead to more monodispersed valency. B) Bluk dynamics is contractile at high motor concentrations ([Motor clusters]=480nM, [ATP]=30µM, [Tubulin]=1.33mg/mL). C-D) In similar conditions, single Microtubule microscopy reveals that clusters of K365 end-accumulate. C shows labeled tubulin in cyan, and D shows labeled motor clusters in orange. E) Time-lapse imaging reveals that K365 motor clusters are highly processive. The run length is longer than 4µm.

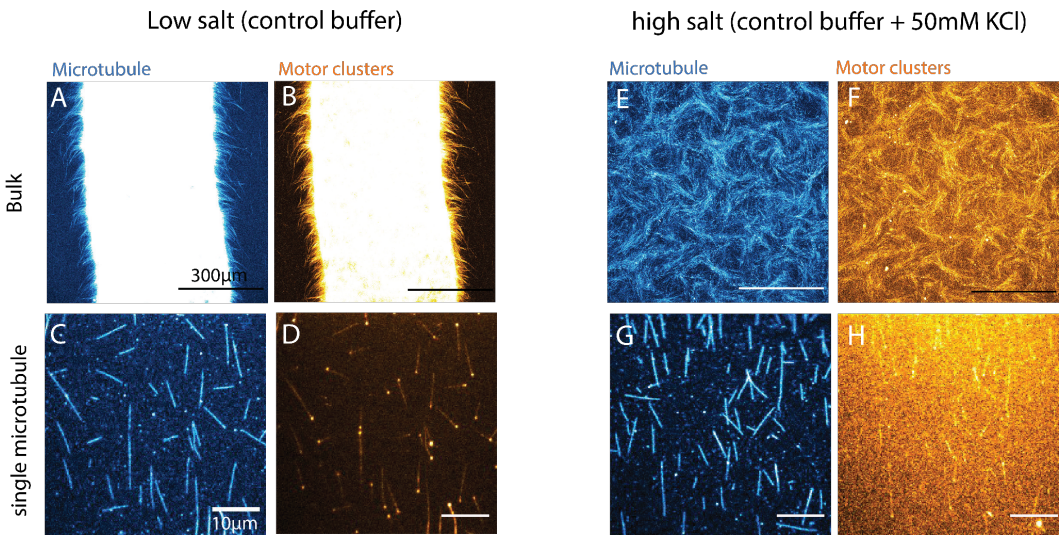

Figure S7: Decreasing the residence time of motors onto microtubules drives the transition from contractile to extensile. In the absence of KCl (control), the active gels (A) tubulin channel, B) motor channel) globally contracts and motor clusters accumulate at the end of the microtubule (C) tubulin channel, D) motor channel). Adding 50nM of KCl drives bulk extensile dynamics (E) tubulin channel, F) motor channel) and motor caps disappear (G) tubulin channel, H) motor channel). A-H were taken with a confocal microscope. Scale bar in A, B, and F is 300 µm. Scale bar in C, D, G, and H is 10 µm. In all experiments, [ATP]= 30µM, [motor clusters]= 480 nM. Both bulk and single microtubule experiments were performed in 3 independent replicates.

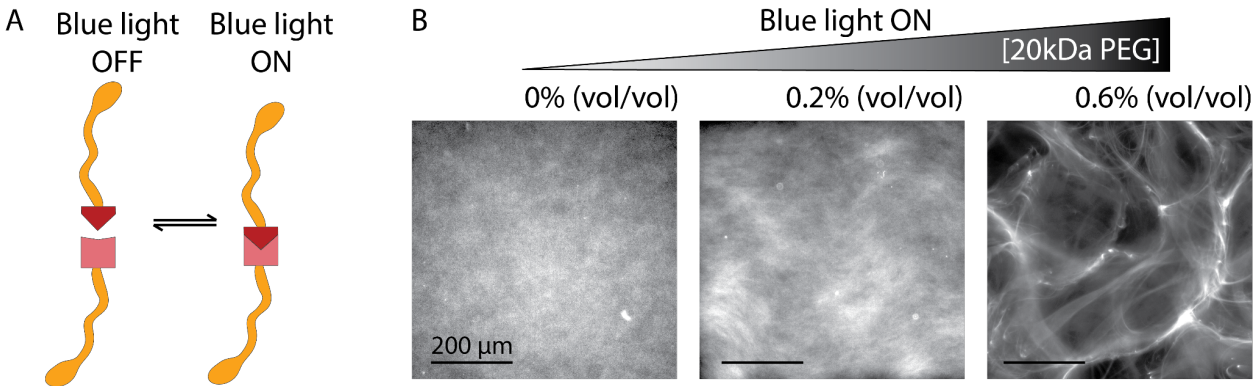

Figure S8: Dimers of K365 do not form asters. A) schematic of the light-dimerizable single-headed opto-K365 motors. When the light is off, the motors are not dimerized. When the blue light is on, the motors dimerize. B) Fluorescent pictures of the active gels composed of 500nM of each iLid and micro motors. In the absence of PEG, no motion is observed. Adding PEG increases the depletion interaction and extensile motion is detected. ([ATP]=30µM, [MT]=1.33mg/mL). Experiments were performed in 3 independent replicates.

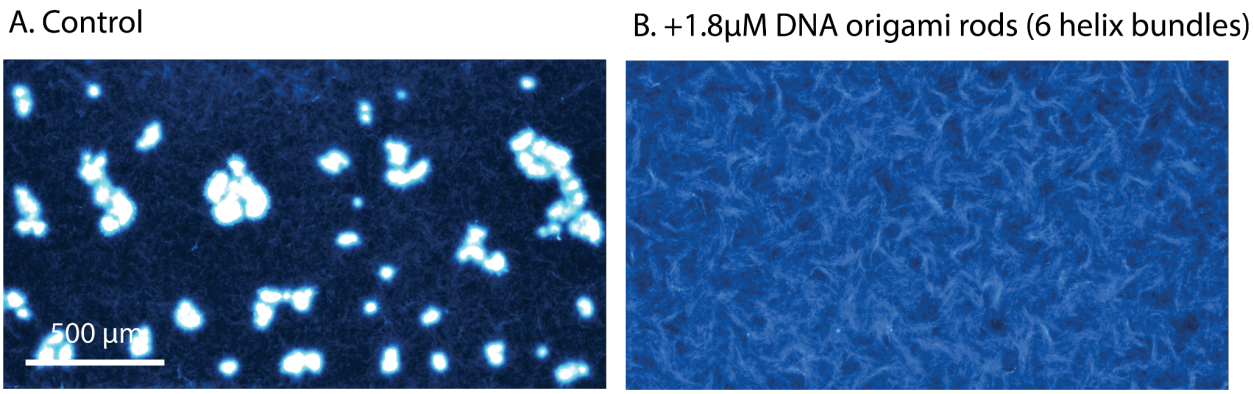

Figure S9: Adding 6-helix-bundles DNA origami rods turns a contractile phase extensile. A) Control is contractile, B) and turns extensile when 1.8uM of DNA rods are added. [ATP]=30μM, [Motor cluster]=400nM, [PRC1]=100nm, [MT]=1.3mg/mL

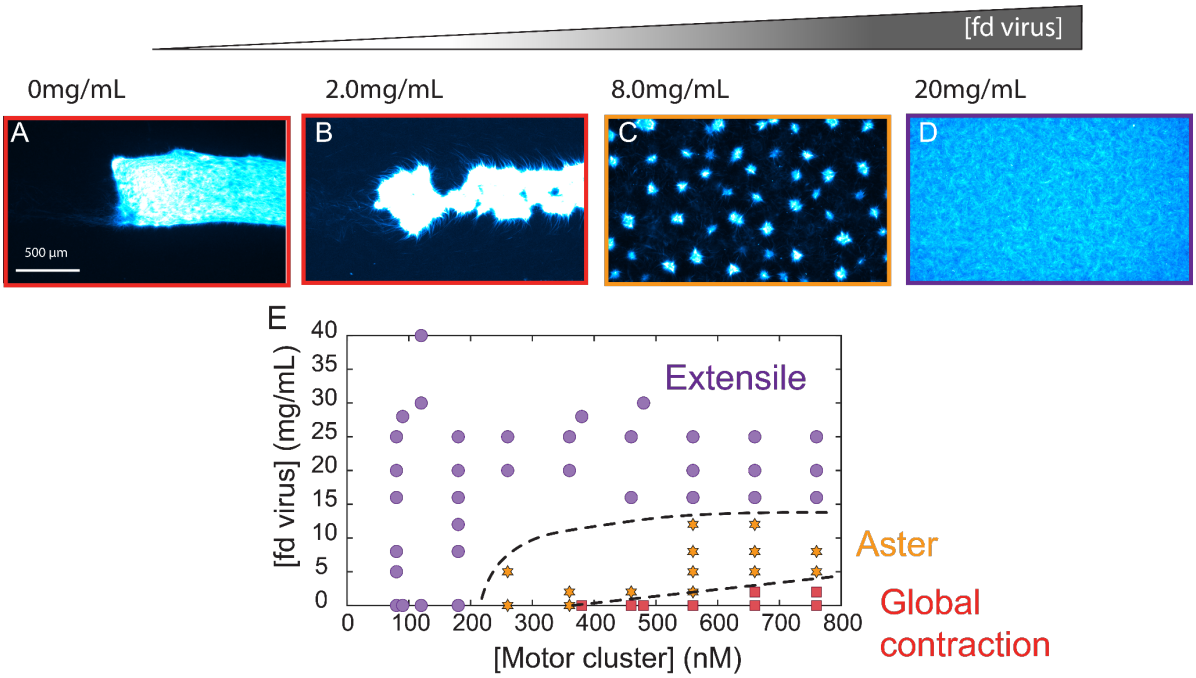

Figure S10: Effect of increasing nematic alignment by adding *fd* viruses in the background. A-D) fluorescent images when *fd* was added at 0, 2, 8, and 20mg/mL. The globally contractile phase turns first into an aster phase, and then into the extensile phase when more *fd* viruses are added. E) *fd*-Motor cluster phase diagram. Dash phase boundaries are a guide for the eye.

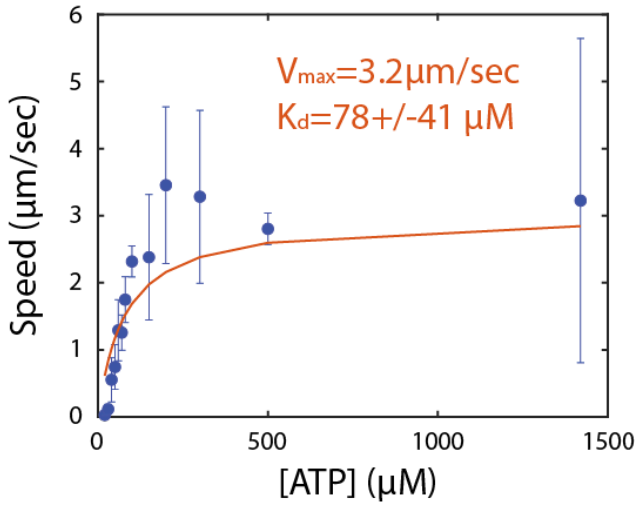

Figure S11: Estimation of K_d by fitting the speed vs ATP plot to a Michaelis-Mentel model. Error bars: standard deviation over 4 independent replicates. Blue points: experimental data points, red line: best fit of $V=V_{max}/(K_d+[ATP])$.

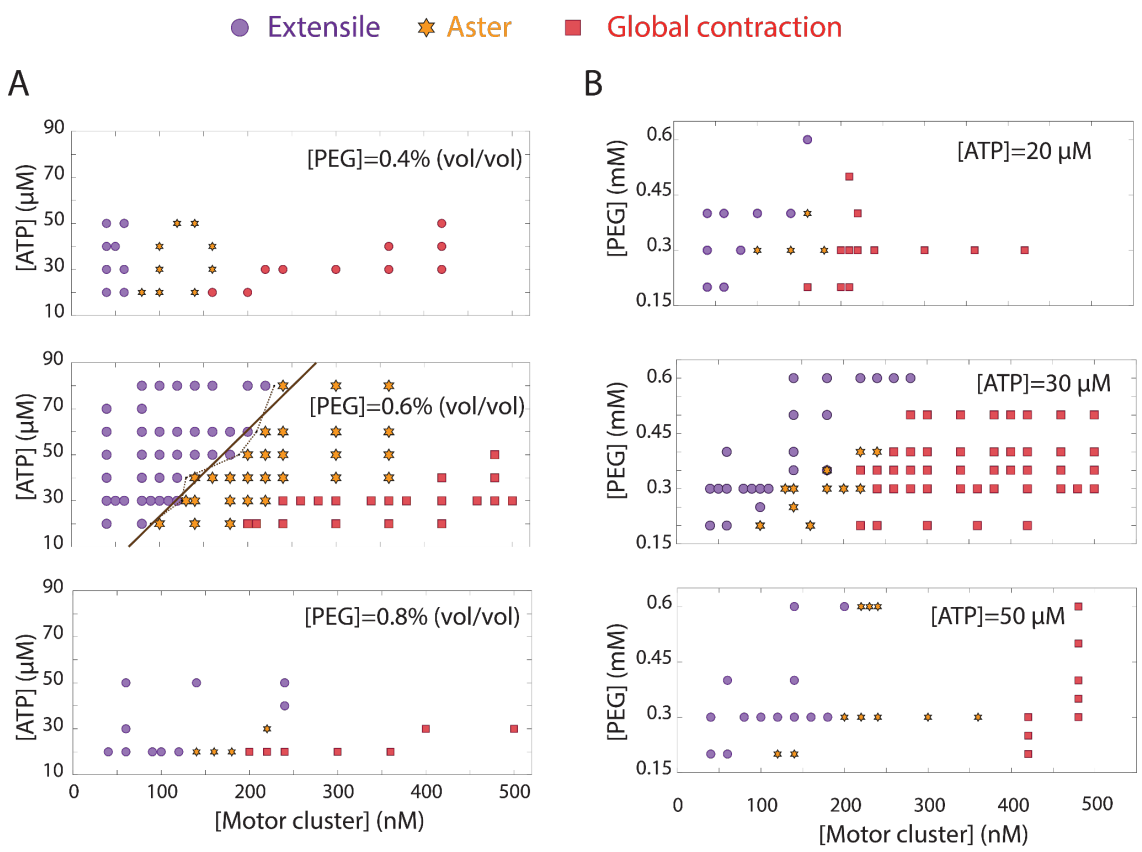

Figure S12: Summary of all the 2D phase diagrams collected for this study. A) ATP-motor cluster phase diagrams for various PEG concentrations. B) PEG-motor cluster phase diagrams for various ATP concentrations. [Tubulin]=1.33mg/mL for all experiments reported in these 6 phase diagrams. The dashed line corresponds to the experimental phase boundary to which the model (continuous line) is fitted.

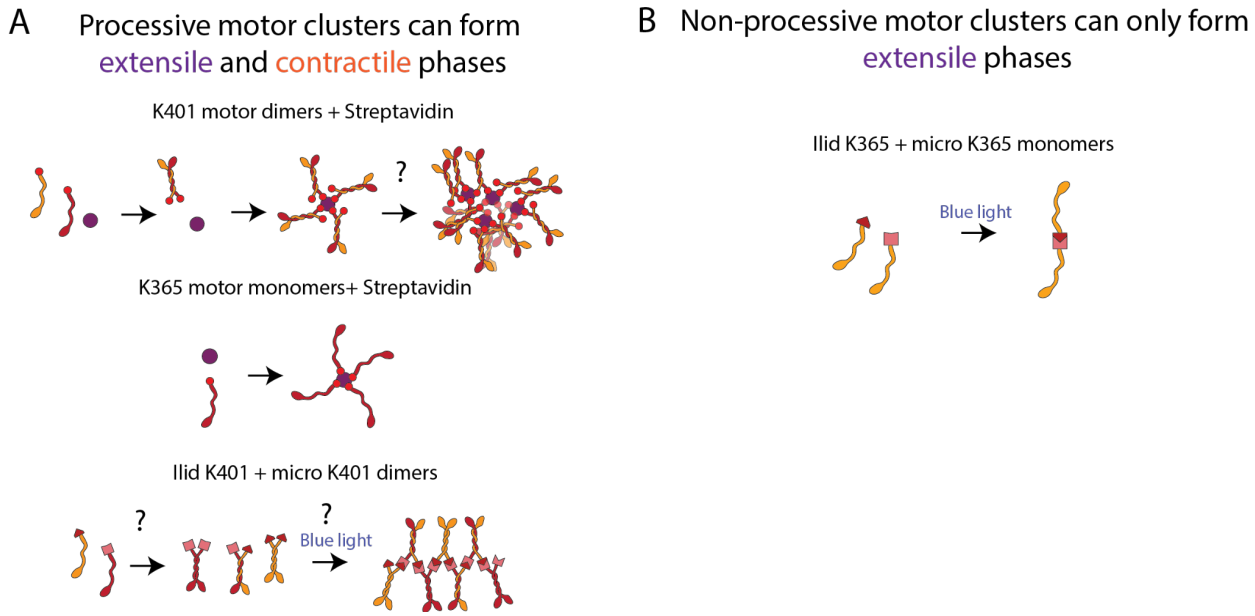

Figure S13: Valency of the motor clusters controls the self-organization of the kinesin-microtubule gels. A) multivalent clusters can drive extensile and contractile dynamics because the clusters are highly processive and have the ability to end-accumulate under the right experimental conditions. B) However, non-processive clusters cannot end-accumulate and therefore cannot form asters. These motors can only drive extensile dynamics.

7. Caption Supplementary videos

Video S1: extensile chaotic phase in an active network of microtubule and kinesin motor clusters. [ATP]=30µM, [motor cluster]=60nM, confocal microscopy, microtubules labeled with Alexa 647.

Video S2: aster phase in an active network of microtubule and kinesin motor clusters. Asters locally contract while the background is still extensile. [ATP]=30µM, [motor cluster]=120nM, confocal microscopy, microtubules labeled with Alexa 647.

Video S3: globally contractile phase in an active network of microtubule and kinesin motor clusters. [ATP]=30µM, [motor cluster]=480nM, confocal microscopy, microtubules labeled with Alexa 647.

References for Supplementary Materials

[1] M. Castoldi and A. V. Popov, Protein Expression and Purification **32**, 83 (2003).
[2] T. Sanchez, D. T. Chen, S. J. DeCamp, M. Heymann, and Z. Dogic, Nature **491**, 431 (2012).
[3] S. J. DeCamp, G. S. Redner, A. Baskaran, M. F. Hagan, and Z. Dogic, Nature Materials **14**, 1110 (2015).
[4] R. Subramanian, E. M. Wilson-Kubalek, C. P. Arthur, M. J. Bick, E. A. Campbell, S. A. Darst, R. A. Milligan, and T. M. Kapoor, Cell **142**, 433 (2010).
[5] P. Chandrakar *et al.*, Soft Matter **18**, 1825 (2022).
[6] D. S. Martin, R. Fathi, T. J. Mitchison, and J. Gelles, Proc. Natl. Acad. Sci. U. S. A. **107**, 5453 (2010).
[7] T. D. Ross, H. J. Lee, Z. Qu, R. A. Banks, R. Phillips, and M. Thomson, Nature **572**, 224 (2019).
[8] L. M. Lemma, M. Varghese, T. D. Ross, M. Thomson, A. Baskaran, and Z. Dogic, arXiv preprint arXiv:2209.06277v1 (2022).
[9] M. P. Nicholas, L. Rao, and A. Gennerich, Methods Mol Biol **1136**, 137 (2014).
[10] A. D. Edelstein, M. A. Tsuchida, N. Amodaj, H. Pinkard, R. D. Vale, and N. Stuurman, J. Biol. Methods **1** (2014).
[11] W. S. Rasband, US National Institutes of Health, Bethesda, Maryland (1997–2012).
[12] W. Thielicke and E. J. Stamhuis, *PIVlab - Time-Resolved Digital Particle Image Velocimetry Tool for MATLAB* 2014), Vol. 132.